Tear Film Thickness and its Effects on the Recording of Multi-electrode Electroretinographic Responses

BY

MATTHEW ELLIS
B.S., Northern Illinois University, 2010

THESIS

Submitted as partial fulfillment of the requirements
for the degree of Master of Science in Bioengineering
in the Graduate College of the
University of Illinois at Chicago, 2014

Chicago, Illinois

Defense Committee:

John Hetling, Advisor and Chair
Hananeh Esmailbeigi
Timothy McMahon, Ophthalmology

TABLE OF CONTENTS

TABLE OF CONTENTS *(continued)*

LIST OF TABLES

LIST OF FIGURES

LIST OF FIGURES (***continued***)

FIGURE PAGE

LIST OF EQUATIONS

LIST OF ABBREVIATIONS

ERG	Electroretinogram
CLEAr	Contact Lens Electrode Array
meERG	Multi-electrode electroretinogram
mfERG	Multi-focal electroretingram
OCT	Optical Coherence Tomography
PCTF	Pre-corneal Tear Film
PDMS	Polydimethylsiloxane
PLTF	Pre-lens Tear Film
PMMA	Poly(methyl methacrylate)
PoLTF	Post-lens Tear Film
QI	Quality Index
SNR	Signal-to-noise ratio

1. SPECIFIC AIMS

1.1 Problem Statement

Glaucoma is a progressive neurodegenerative disorder in which ocular stressors adversely affect retinal ganglion cells, causing dendritic and axonal atrophies that eventually lead to cell death and irreversible loss of vision. It is estimated that by the year 2020 the disease will affect more than 80 million individuals worldwide (Quigley and Broman, 2006). Thus the effective management of glaucoma represents a critical, unmet medical need. Toward this end, the irreversible nature of glaucomatous vision loss dictates that the disease must be detected early in its progression if the efficacy of treatment plans is to be maximized. However, the early detection of glaucoma remains a difficult task. To overcome this challenge, the novel technology behind multi-electrode electroretinography has been developed by Dr. John Hetling of the University of Illinois at Chicago. This novel approach to elecroretinography uses a **C**ontact **L**ens **E**lectrode **Ar**ray (**CLEAr** Lens™) to record spatially distinct bioelectric potentials from the cornea. These biopotentials are then used to interpret the health of the retina. It is hypothesized and supported by early data that via this approach, spatially localized functional deficits, such as those associated with glaucoma, can be detected at early stages of disease progression.

The technique of multi-electrode electroretinography is dependent upon the recorded corneal potentials being *spatially distinct.* That is, the signals must preserve unique information about the underlying source currents generated by retinal activity (see Figure 4). However, such information is lost if the signals are shunted together, which may occur if tear film between the cornea and recording lens is too thick. This places particular importance upon the thickness of this tear film with respect to the multi-electrode electroretinogram (meERG) project. Thus, this Thesis will be focused upon studying the dynamics of the tear film thickness beneath the CLEAr Lens. Through measuring tear film thickness in the ~20 minutes that follow lens insertion, we seek to investigate how tear film thickness affects meERG recording. We hypothesize that following lens insertion, there is a lens-settling period over which tear film thickness changes. Furthermore, we hypothesize that these changes in tear film thickness will induce predictable alterations in meERG responses. To examine these hypotheses, the current study seeks to determine how tear film thickness changes over the course of the lens settling period, and how these

changes are manifested in meERG responses. To accomplish these goals, the project has been divided into the following Specific Aims.

1.2 Specific Aims

I: Develop a CLEAr Lens analog that closely matches the geometric and mechanical properties of the CLEAr Lens, and provides the necessary optical clarity to accurately image tear film through.

II: Measure the thickness of the tear film beneath a CLEAr Lens analog during the lens-settling period. These measurements will be taken over a 20-minute window following lens insertion and will be acquired via optical coherence tomography (OCT).

III: Record multi-electrode electroretinogram responses over a 20-minute time window following CLEAr Lens insertion and analyze the data for lens-settling effects. This analysis is expected to guide us in evaluating the correlation between tear film thickness and multi-electrode electroretinogram responses and outlining a means to monitor the lens settling process using only meERG response data.

1.3. Project Significance

Through probing the correlation between tear film thickness measurements and temporally matched meERG responses, the present study seeks to provide quantitative information that will aid in the refinement of meERG recording protocols. During the lens settling period, meERG responses are altered by changes in tear film thickness, and since these alterations come from non-retinal sources, they diminish the ability of multi-electrode electroretinography to functionally assess the health of the retina. Thus, a primary goal of this study is to formulate a method that allows us to evaluate meERG responses and infer tear film thickness. Furthermore, it is expected that the analysis performed here will pave the way toward establishing on-line method of monitoring the lens settling process, thus allowing tear film thickness to be assessed during the course of a meERG recording session.

2. INTRODUCTION

2.1. Electroretinography

2.1.1. Overview of Electroretinography

Electroretinography is a clinically accepted means of inferring retinal function from biopotential measurements taken at the cornea. When light strikes the photosensitive neurons in the retina, information about the visual scene is transduced into electrical activity, processed by a network of retinal neurons, and transmitted to the brain via the optic nerve. This electrical response, initiated by the movement ions into or out of retinal neurons, leads to the generation of electric fields that propagate in all directions. Upon reaching the cornea, these electric fields summate, and can be measured via corneal electrodes. This is the practice of electroretinography and the output waveform is termed the electroretinogram (ERG).

2.1.2. Retinal Signal Processing and the Electroretinogram

To comprehend the ERG waveform one must peer beneath the cornea and examine the retinal sources that generate it. After light strikes the retina, a signal-processing cascade is initiated that transforms light input into a neural signal that can be decoded by the brain. This signal cascade consists of three primary steps. The excitatory neurons that transmit information between the steps have been italicized below and in highlighted in red in Figure 1. It should also be noted that numerous modulatory neurons are contained within the retinal circuitry; these inter-neurons are referred to as horizontal and amacrine cells and can also be seen in Figure 1.

Retinal Signaling Cascade:

1. Upon exposure to a change in luminance, *photoreceptors* (i.e. rods and cones) respond by changing their membrane potential in a graded manner. This change in membrane potential causes a graded change in the rate at which the photoreceptors release neurotransmitter, which is glutamate for the excitatory neurons discussed here.

2. Through varying the rate of glutamate release, photoreceptors faithfully transmit a graded response to the retina's second order neurons, called *bipolar cells*[1]. The bipolar cells in turn respond with a graded change in membrane potential. Similarly to the photoreceptors, bipolar cells also vary their rate of glutamate release in response to changes in membrane potential.
3. Next, bipolar cells transmit information to the retina's tertiary neurons, *retinal ganglion cells*, which are the output cells of the retina. Retinal ganglion cells integrate the upstream bipolar cell inputs, and should a threshold be crossed, they fire action potentials down the optic nerve. Note, retinal ganglion cells are not graded neurons. Their membrane potential deflections occur in the form of *rapid* and *transient* action potentials. This is opposite to light responses of photoreceptors and bipolar cells, whose membrane potential variations are *slower* and *graded*.

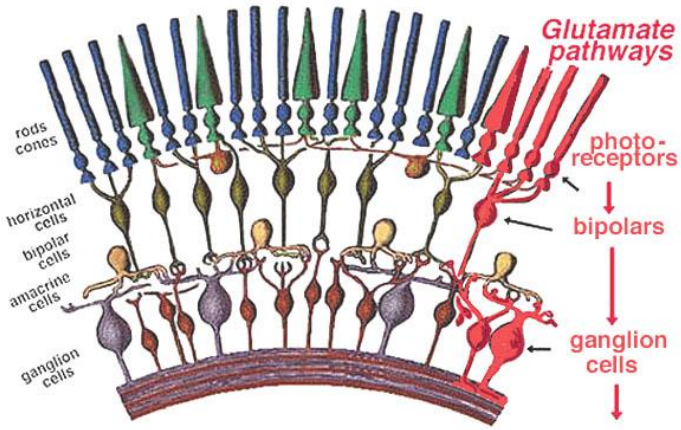

Figure 1: Summary of excitatory transmission through the retina. The excitatory neurons corresponding those in the above signaling cascade have been highlighted in red text on the right. Reproduced with from http://webvision.med.utah.edu/, there is no permission necessary for academic use; see website for details.

With these three steps in hand, we are now in a position to discuss how the retinal sources manifest themselves in the ERG waveform. Importantly, each step of the retinal signal cascade occurs at temporally distinct points. The photoreceptors respond before the bipolar cells, and the bipolar cells before the ganglion cells. While these signaling events do exhibit a large degree of temporal overlap,

[1] Bipolar cells can be segregated into two categories: ON bipolar cells and OFF bipolar cells. ON bipolar cells respond to increments of light whereas OFF bipolar cells respond to decrements of light. However in the following discussion will be limited to ON bipolar cells, because their contribution to the full field ERG dominates that of the OFF bipolar cells.

each step produces a notable, temporally distinct feature in the ERG waveform. Detecting and quantifying these features forms the basis of ERG analysis. In what follows, ERG analysis in response to a brief (<1ms), full field, flash of light, will be examined by correlating features in the ERG waveform with the retinal signal-processing cascade.

When light strikes the photoreceptors their membrane potential hyperpolarizes (*step one*). This causes a negative-going deflection in ERG and is termed the *a-wave* (Figure 2). In response to photoreceptor hyperpolarization, the flow of glutamate upon bipolar cell synapses is reduced. This reduction in glutamate then initiates a depolarization of ON bipolar cells, which manifests itself as a positive-going deflection in the ERG response (Figure 2). This is called the *b-wave.* Following the b-wave the ERG waveform slowly returns to baseline. Note that the ganglion cell response (*step three*) is conspicuously absent from this interpretation; this is due to the fact that ERGs elicited by full field stimuli do not produce a measureable ganglion cell response (Bui and Fortune, 2003). Nonetheless, ERGs elicited by more diverse stimulus patterns do indeed produce a measurable ganglion cell response; this will be discussed in the following section[2].

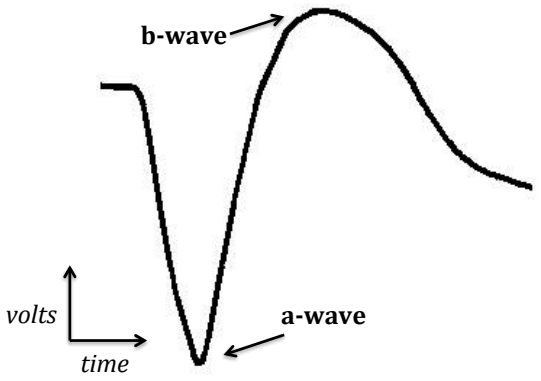

Figure 2: Example ERG waveform. The a- and b-waves are highlighted. The absence of scale bars is intentional; this figure is meant to be illustrative and not quantitative.

[2] This discussion of ERG features was intentionally brief because the analysis conducted as part of this Thesis uses only the a- and b-waves. For a more thorough overview of the ERG and its features see the articles about electroretinography at http://webvision.med.utah.edu/.

2.1.3. Clinical Applications of the Electroretinogram

Conventional electroretinography utilizes a single electrode to record the summated electrical activity generated by the entire retina (Figure 3A). By dissecting the ERG waveform in the features mentioned above, this approach can be used to assess the health of *entire* populations of retinal neurons. It is in this regard that the ERG maintains considerable clinical relevance, and allows blinding eye diseases to be diagnosed and monitored via electroretinography. An example of such a disease is retinitis pigmentosa, an inherited disease in which genetic mutations affect the health of the retina's rod photoreceptors (Phelan and Bok, 2000). Since this disease affects the photoreceptors, one would expect the a-wave recorded from retinitis pigmentosa patients to be distorted. Indeed this is the case; studies have shown that the a-wave occurs with increased latency in retinitis pigmentosa patients (Berson, 1993).

Retinal dysfunction induced by glaucoma can also be assessed by electroretinography. However, glaucoma is a disease that primarily affects retinal ganglion cells. Thus ERGs obtained via uniform, full field stimulus presentation offer limited utility in this pursuit. To evoke a measurable ganglion cell response in the ERG waveform, stimuli containing contrast-reversing patterns (e.g. checkerboard) or chromatic opposition (e.g. a blue flash on a yellow background) must be used instead. The use of a contrast-reversing checkerboard to evoke ERGs is referred to as *pattern electroretinography*, and has been shown to offer efficacy toward monitoring the progression of glaucoma (Bach *et al*., 2006). Through the use of chromatically opposed stimuli, an ERG component referred to as the photopic negative response can be evoked, and reduction in this component has been correlated with glaucomatous damage (Viswanathan *et al.*, 1999).

2.2 Multi-electrode Electroretinography

2.2.1. Basics of Multi-electrode Electroretinography

Conventionally recorded ERG responses allow the health of the *entire* populations of retinal neurons to be assessed. However, blinding eye diseases such as glaucoma exhibit patterns of *spatially localized* damage (Nickells *et al.*, 2012). In light of this, conventional ERG approaches used to diagnose glaucoma

offer limited effectiveness. It is a plausible and unfortunate scenario that conventional electroretinography could fail to detect a significantly diseased region of the retina because the healthy retina that surrounds it will dominate the ERG response and mask the severity of the damage. Thus, when monitoring the progression of, and/or diagnosing glaucoma, a means of assessing the spatial extent of the damage would prove very beneficial. Toward the pursuit of this goal, the Neural Engineering Vision Laboratory (NEVL), led by Dr. John Hetling, has been developing a novel electroretinographic recording technology that affords the ability to simultaneously record the electrical activity at *multiple locations* across the cornea (Figure 3); this progressive approach toward electroretinography has been coined as the *multi-electrode* electroretinogram (meERG). It is hypothesized that via recording the ERG in this manner, retinal function can be spatially assessed by analyzing the distribution of potential differences across the corneal surface. Driving this hypothesis is the notion the activity generated in different regions of the retina will propagate to the same corneal location with varying strengths. Accordingly, the potential recorded at a known position on the cornea can be interpreted as a weighted sum that depends on retinal source location (for an illustration of this concept, see Figure 4C).

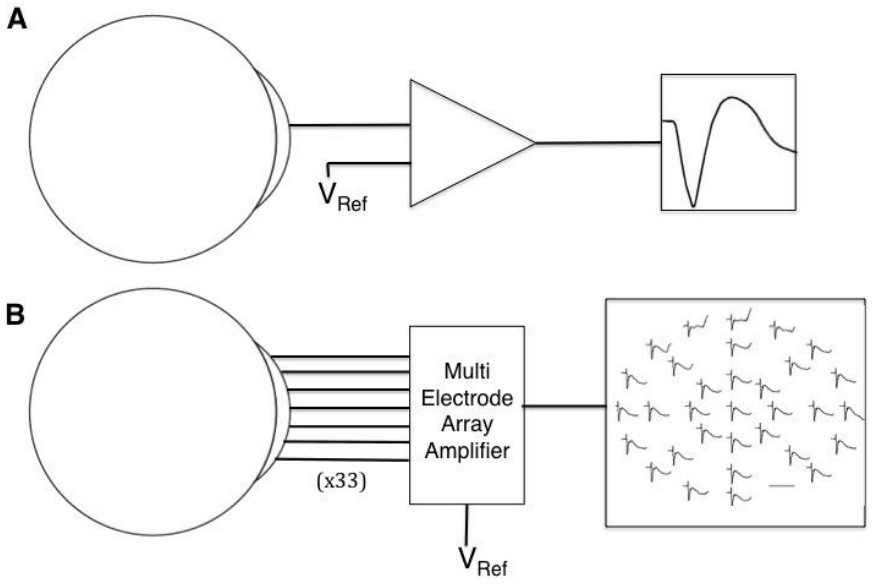

Figure 3: Differences between electroretinography and multi-electrode electroretinography. Both systems go from cornea to amplifier to computer. (A) Schematic of signal recording in conventional electroretinography and a sample waveform. (B) Schematic of recording setup used in multi-electrode electroretinography.

To facilitate the recording of multiple potentials from the ocular surface, an electrode array must be opposed to the surface of the eye. This is accomplished via an engineered contact lens made from poly(methyl methacrylate) (PMMA) that houses an electrode array (Figure 4A and B); throughout the remainder of this work the contact lens will be referred to as the **C**ontact **L**ens **E**lectrode **Ar**ray or **CLEAr** Lens™. Currently, the meERG project has successfully prototyped a recording system using the CLEAr Lens and a multi-electrode array amplifier, and validation experiments are now underway.

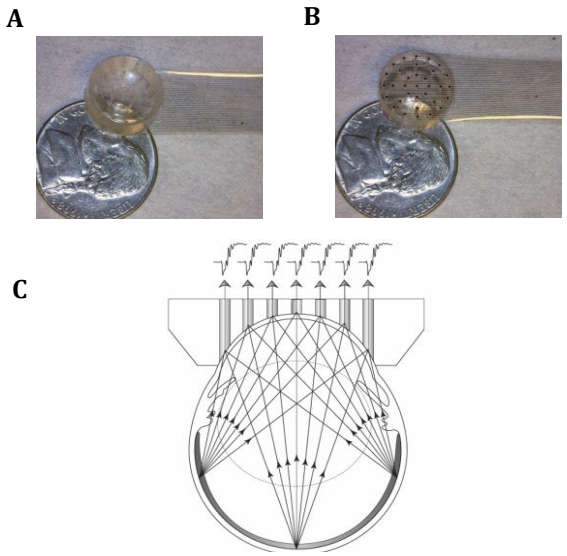

Figure 4: Recording of multiple bioelectric potentials from the corneal surface. (A) and(B) show photographs of the CLEAr Lens with cable attached. Above each of the through-holes is a gold electrode that forms a conductive path from cornea to amplifier. (C) An illustration of how ERG signals generated at different retinal locations propagate to different cornea with varying strengths. Illustration in (C) courtesy of Dr. Amani Al-Tarouti.

2.2.2. Potential Clinical Advantages

Currently, when deficits in retinal dysfunction cannot be detected electrophysiologically, ophthalmologists must rely of structural and/or psychophysical means of detecting visual maladies. These approaches, however, are limited in that they fail to provide a correlate to retinal function, leaving ophthalmologists to infer the extent of retinal damage. Furthermore, it has been shown that in the case of glaucoma, retinal dysfunction precedes both structural damage and visual field loss (Banitt *et al.*, 2013). In this respect, glaucoma is often referred to as the ‘silent thief of sight’. The disease progresses unknowingly until the damage becomes apparent; and since glaucomatous damage is currently irreversible, a diagnosis at this

point it is often too late to treat the disease effectively. This underscores the need to detect glaucoma, and other blinding eye diseases, early in their progression. It is from this critical need that the meERG project was born.

Through a successful validation of multi-electrode electroretinography, we seek to spatially interpret retinal function from an array of corneal potentials; much akin to how electroencephalography uses biopotentials recorded across the scalp to infer brain function. Through this novel interpretation of corneal potentials, it is anticipated that deficits in retinal function not detectable by conventional electroretinography methods can be successfully detected via multi-electrode electroretinography. Therefore, by affording the ophthalmic community with a novel means of early detection, multi-electrode electrode electroretinography seeks to change the way retinal degenerative diseases are diagnosed.

2.3. Multi-electrode Electroretinography and the Importance of Tear Film Thickness

To successfully infer retinal function from array of corneal potentials, one must be cognizant of how the electric fields generated in the retina propagate to the recording electrodes. This involves quantitative knowledge about the geometry and electrical conductivity of the ocular tissues. Toward the acquisition of such knowledge, previous NEVL lab members developed a finite element model to mathematically depict the propagation of electric fields through the eye. While those results are very telling as to what happens to the signal as it propagates from the retina to the cornea, the available quantitative information provided little insight as to what happens after the signal leaves the cornea. That is, they used an assumption that the tear film between the cornea and recording electrodes is a fixed thickness, referring to literature that reported a constant tear film thickness (King-Smith et al, 2004). This fails to accurately reflect the CLEAr Lens case, as tear film thickness underneath a contact lens, in the absence of blinking, has yet to be studied from a dynamic perspective. This gap in knowledge raises an important issue in regards to the acquisition and analysis of meERG signals; we cannot create an accurate map of retinal function if we are unsure of how thick the tear film is when the measurements are acquired. Thus the principle aim of this work will be devoted toward the study of how the tear film thickness changes following insertion of the CLEAr Lens, and the effect that these changes have on meERG responses.

3. BACKGROUND

3.1. Composition of Tear Film

Forming the outermost layer of the ocular surface, the tear film plays an important role in keeping the cornea hydrated, lubricated, and free of debris. In terms of its structure, the tear film is thought to consist of three distinct layers: a hydrophilic adhesion layer, an aqueous layer, and a lipid layer (Figure 2), with each layer having a particular function (Braun, 2012). To keep the eye hydrated, the corneal surface must possess the quality of wettability; this is accomplished via a glycocalyx layer secreted by the cornea's epithelial cells (Sharma, 1998). Atop this hydrophilic glycocalyx layer sits an aqueous layer that most people commonly refer to as tears. While the aqueous portion of the tear film is said to be 98% water, the remaining two percent consists of soluble salts and gel-forming mucins that are vital to maintaining the health of the ocular surface (Gipson, 2004). The outermost portion of the tear film is a lipid layer that performs two important tasks: it slows evaporation of the underlying aqueous tear fluid, and allows the tear film to function as a smooth optical surface (Bron *et al.,* 2004).

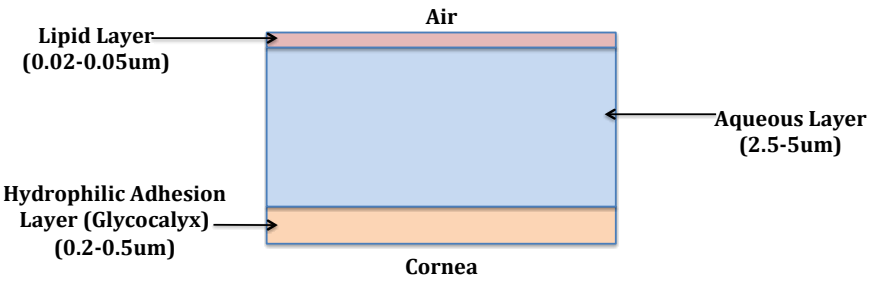

Figure 5: Tear film is composed of three distinct layers. The three layers are denoted by different colors, which the approximate thicknesses shown in parentheses below (note, figure is not to scale). The thicknesses used above are taken from Braun (2012).

Taken as a functional unit, the tear film provides important mechanisms by which ocular health and comfort are maintained. However, if the tear film is compromised, the results can be quite irritating. A noteworthy example is the case of dry eye disease, which causes painful irritation on the surface of one's eye. Resulting from diminished tear film stability, dry eye disease can produce a hyperosmolarity of the tear film, ultimately leading to inflammation of the ocular surface (Smith, 2007). Furthermore, if dry eyed disease is not managed effectively, it can lead to symptoms of blurred or foggy vision (Begley *et al.,* 2003), thus underscoring the importance of the tear film.

3.2. Tear Film Thickness—No Contact Lens

With tear film playing a crucial role in the maintenance of ocular health, considerable effort has been made to assess the health of one's tear film. Toward this end, low-cost devices capable of measuring tear film thickness have recently emerged as a clinically viable means of monitoring the health of the ocular surface (Azartash *et al.,* 2011; Korb *et al.* 2012). However, before technological advancements allowed tear film thickness measurements to become clinically accessible, researchers conducted numerous studies attempting to quantify tear film thickness (for a thorough review, see King-Smith *et al.* 2004). These studies investigated tear film thickness across numerous species and utilized an array of techniques. While the methods used were often laborious and invasive, they provided a fertile foundation from which our knowledge of the tear film has advanced considerably.

Results from the first attempt to measure the thickness of tear film in humans were published in 1965; this was accomplished by placing absorbent paper discs upon the cornea and found the thickness of human tear film to be 7 µm (Ehlers, 1965). While providing the ophthalmic community the first quantification of human tear film thickness, the study possessed one noteworthy drawback. The measurements were static and not dynamic. Every time we blink, the tear film is replenished, and spreads about the corneal surface to evenly coat the eye. While illuminating, the results provided by Ehlers fail to describe the dynamic nature of the tear film. New techniques allowing for the dynamic measurement of tear film thickness were needed to more thoroughly investigate this issue. Initially, these advances came in the form of flurometric measurements (Benedetto *et al.,* 1975). Via flurophotometry, Benedetto *et al.* provided evidence that the tear film's thickness depends on both corneal position and time after a blink.

To this day, fluorometry is clinically used to evaluate contact lens fitting (Tan *et al.,* 2013). This would seemingly make flurometry an attractive method to consider for the current project. Especially given the fact that a prior study had used fluorometry to quantitatively measure tear film thickness beneath a contact lens placed atop a model eye (Holt, 1997). However, the work by Holt differs significantly from the

current study in that it did not include dynamic measurements, nor were the measurements obtained *in vivo*. These notable distinctions severely limit the efficacy of flurometric measurements in our case.
To quantitatively measure tear film thickness fluorometrically, the concentration of fluorescein dye must be known; this is dependent on the volume of tear film, which *in vivo* can change upon lens insertion. Moreover, to perform these measurements dynamically, one must know the rates of tear film evaporation and replenishment. These quantities can vary significantly across individuals and cannot be accurately determined. Thus, due to quantitative limitations, fluorometric measurements were not used to dynamically measure tear film thickness in this Thesis.

As the field of optics advanced increasingly elegant methods to dynamically measure tear film thickness began to emerge. In this regard, the method of interferometry became prevalent. By making clever use of the fact that the tear film is a different index of refraction than sandwiching media of air and cornea, the interferometric approach offers a particularly efficacious method to investigate tear film thickness. Using interferometry, tear film thickness in human was found to be 2.7 μm (King-Smith *et al.,* 2000). Despite these apparent advantages of good spatial resolution (~1 μm) and a high signal-to-noise ratio (up to roughly 200) (King-Smith *et al.,* 2004), interferometry suffers from limited clinical viability. The optical setup is prohibitively expensive and very time consuming to maintain. Nonetheless, tear film thickness remains a clinically important metric. Toward this end, more accessible means of tear film measurement have been pursued.

Optical coherence tomography was first developed for *in vivo* retinal imaging and remains widely used by the ophthalmic community. In addition, it serves as a viable modality to image the anterior segment of the eye. Thus, the potential of OCT to resolve the thickness of the tear film has been investigated through multiple studies (Wang et al, 2003; Wang et al, 2009; Chen et al, 2010). The capability of OCT to perform in this capability was first demonstrated by Wang et al. in 2003. They found the tear film thickness to be 3.3 μm (Wang et al, 2003), a result that closely matches the thickness of 2.5 μm measured by King-Smith et al.(2000). Furthermore, recent studies have used OCT to monitor the *dynamic* changes of tear film thickness following contact lens insertion (Wang et al, 2009; Chen et al, 2010). In light of this work and

the widespread use of OCT by the ophthalmic community, we have chosen to employ OCT as our principle method of investigation of tear film thickness (see Methods).

3.3. Tear film Thickness—Conventional Contact Lens

Following the insertion of a contact lens the tear film is compartmentalized into two regions separated by the contact lens: a pre-lens tear film (PLTF), which sits between the lens's outer surface and the air, and a post-lens tear film (PoLTF), that sits between the cornea and the lens's inner surface (Figure 6)**.** To describe the tear film in the absence of a contact lens, the term pre-corneal tear film (PCTF) is used. Thus far, the PCTF has been referred to as 'tear film'. Correspondingly, to make clear distinctions across these different tear films, the term 'tear film' will no longer be used unambiguously.[3]

Upon lens insertion, the ocular surface is exposed to an external stressor. In response to this stress, biophysical properties of both the PLTF and PoLTF are altered. This subsection will be focused primarily upon the PoLTF, as it constitutes the final layer through which meERG signals must traverse before being collected by the recording electrodes. Specifically, contact lens induced stress can produce changes in PoLTF stability, rate of evaporation, and osmolarity (Craig *et al.,* 2013). Importantly, alterations in these biophysical properties are all related to one another. And furthermore, they all have an effect on tear film thickness. Therefore, the time-dependent changes in PoLTF thickness resulting lens insertion will be discussed according to the underlying biophysical mechanisms that produce them.

This viewpoint of PoLTF thickness is unique. Under normal contact lens wear, the thickness of the PoLTF is governed by blinking. However, in the CLEAr lens case, blinking does not occur. This represents a peculiar scenario as PoLTF dynamics in the absence of blinking have yet to be thoroughly investigated. Despite the uniqueness of the CLEAr Lens scenario, parallels to other studies can still be drawn. It was recently demonstrated that following lens insertion, PoLTF thickness depends on whether

[3] This is to say that the term 'tear film' will be used in reference toward either the PCTF, PLTF, or PoLTF. Such a distinction should be made clear by the surrounding text.

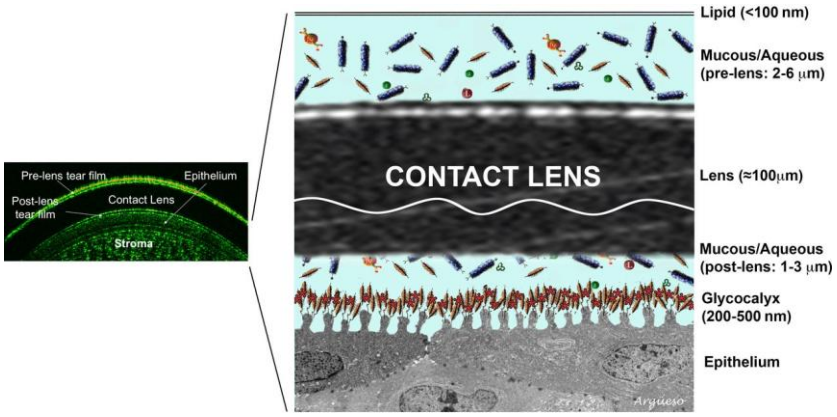

Figure 6: Contact lens the tear film. Left: An OCT image showing a contact lens *in situ*. Note the pre-lens tear film, which sits between air and the contact lens, and the post-lens tear film, which occupies the space between the corneal epithelium and the inner surface of the lens. Right: An illustration magnifying the two layers that stratify either side the contact lens. Interestingly, the lipid layer is absent from the post-lens tear film. Also, the measurements on the right vary considerably from those in Figure 5, this is indicative of contact lens induced tear film alterations, which especially effect the lipid layer. Figure reproduced with permission from Craig *et al.* (2013), copyrights belong to the Association for Research in Vision and Ophthalmology (ARVO).

or not the concave, inner surface of the lens contains a volume of artificial tear solution (Chen et al., 2010). The investigators found that instillation of tear solution in the lens cup caused a marked and transient increase in PoLTF following insertion (Chen et al, 2010). Chen *et al.* (2010) observed that even in the case of thickening by artificial tears, the PoLTF thinned to near baseline levels within 10 minutes, and postulated that excess tear fluid was extruded via blinking. Paralleling the aforementioned study, the instillation of artificial tear fluid upon the CLEAr Lens cup is part of the meERG recording protocol. Contrastingly, however, blinking is not. Thus thinning of the PoLTF underneath the CLEAr Lens must be driven by the biophysical mechanisms mentioned above.

3.4 Novel Considerations For the CLEAr Lens

Due to the prevalence of dry eye disease, tear film dynamics is an emerging area of study (for a review, see Braun, 2012). The tear film is quickly reformed after every blink, producing a smooth optical surface. In this regard, much of the dynamics associated with tear film are owed to blinking. Thus we can think of blinking as the *active* force driving tear film dynamics. However, there also exist *passive* forces, such as diffusion, that play a role in regulating tear film dynamics. While the rapid, frequent nature of the blinking process often relegates these passive forces to a minor role, their importance becomes magnified if the inter-blink interval is lengthened. The CLEAr Lens scenario represents an extreme case of this; the

CLEAr Lens acts as a speculum, inhibiting its wearer from blinking. By removing blinking from the situation, the mixing of the PoLTF with the surrounding PCTF is governed only by passive forces. Of these passive forces, diffusion and convection are hypothesized constitute the primary mechanisms that promote fluid mixing. Additionally, recent evidence has shown that contact lenses made from PMMA can induce corneal swelling (Tyagi *et al.*, 2012). Thus, the swelling of the cornea may also play a role in PoLTF dynamics beneath the CLEAr Lens.

As part of the meERG recording protocol, an ample amount of artificial tear fluid is placed into the concave lens cup prior to insertion. However, it cannot be extruded via blinking as hypothesized by Chen et al. (2010), since the CLEAr lens scenario involves no blinking; it must be extruded passively. Through mixing, the artificial tears coalesce with the PCTF that borders the lens, causing an excess of tear fluid at the edge of the CLEAr Lens. This excess fluid must then be removed from the ocular surface without blinking. In this regard, recent evident has pointed toward evaporation as the primary means by which the PCTF thins between blinks (Nichols et al., 2012). Combining these insights, one can describe the dynamics of the PoLTF in the presence of the CLEAr lens as a two-part process. Initially, diffusion and convection promote mixing of the PoLTF and the surrounding PCTF. Subsequently, the excess tear fluid is removed from the ocular surface via evaporation.

Diffusion and convection represent the two cooperative mechanisms that promote PoLTF mixing in a blink-free scenario. Diffusion can be thought of as statistical process by which concentration gradients are smoothed. Pertaining to the problem at hand, the concentrations we are concerned with are those of salt ions in the tear fluid; specifically, this brings up the notion of osmolarity. Following lens insertion, the tear film on the edge of the lens begins to evaporate, leaving a greater concentration of ions along the edge compared with that of the underlying PoLTF. Osmotic theory predicts that this gradient will be smoothed via diffusion of water from the PoLTF to the bordering PCTF. In this regard, multiple reports have proposed that an osmotic driving force may cause PoLTF depletion (Harris and Mandel, 1969; Little and Bruce, 1995). This is how diffusion is postulated to promote the mixing of tear fluid beneath a contact lens.

Convection, on the other hand, is viewed as a more concerted process, in which the collective properties of large groups of molecules give rise to a bulk flow. In the realm of tear film dynamics, the pertinent property is surface tension. Recalling the preceding discussion, the PCTF was said to evenly coat the corneal surface following a blink. Mechanistically, surface tension gradients between the center of the cornea and the upper eyelid have been found to drive this spread of PCTF (Berger and Corrsin, 1974); this convective spread of fluids in the presence of surface tension gradients is referred to as *Marangoni flow.* In the context of a contact lens, Marangoni flow has been show to impact the thinning rate of the PLTF (Doane, 1988). Doane found that if the edge of the lens contacted the eyelid margins, the PLTF would remain stable and evenly coat the lens surface for roughly 3-6 seconds (Doane, 1988). However, if contact with the eyelids was prevented, the PLTF was found to remain stable for 15-20 seconds (Doane,1988). The rationalization for this was that the PLTF was drawn off the lens's surface via Marangoni flow. Extending these thoughts to the CLEAr lens scenario it is reasonable to figure that Marangoni flow is partially responsible for PoLTF dynamics. Such an effect might be pertinent to our scenario since the CLEAr lens acts as a speculum, and thereby forces the eyelids to rest upon the rim of the lens. Thus, the low surface tension PoLTF is placed in the vicinity of the higher surface tension tear meniscus that resides beneath the eyelid. These conditions allow Marangoni flow to draw the PoLTF from beneath the CLEAr lens.

While diffusion, convection, and evaporation are hypothesized to play a role in the dynamics that govern PoLTF thinning beneath the CLEAr lens, the baseline thickness upon which the PoLTF settles is governed by the fit between the cornea and lens. If the lens is curved too steeply, the PoLTF should be thicker in the center than along the edges and in the case where the curve of the lens is too flat, the PoLTF should be thicker along the edges than in the center. Thus, the method of anterior segment OCT, with its ability to take line scans across the width of the cornea/contact lens interface, offers a promising method by which to investigate lens fit via measuring tear film thickness.

4. METHODS

4.1. Study Design

Our primary goal in this study was to correlate tear film thickness underneath the CLEAr lens analog to temporally matched meERG responses; this is a ***pilot study*** to determine if any notable correlation between the two exists, and if any further investigation is warranted. The correlative nature of the study necessitated the collection of data via two parallel sets of experiments. One experimental branch was concerned with producing a CLEAr lens analog and measuring the tear film beneath it via OCT. The other branch had the goal of collecting time-matched meERG data to correlate with the tear film thickness measurements. Once the data had been collected, we conducted analysis on both data sets and subsequently interpreted how any measured changes in the PoLTF beneath the CLEAr Lens might be affecting the meERG recordings.

4.2. Specific Aim I: Creating a CLEAr Lens Analog

The goal of this Thesis is to dynamically measure the tear film thickness underneath a CLEAr Lens analog and relate these measurements to meERG recording data. It is then reasonable to wonder why the CLEAr lens itself was not used for such experiments. Reasons for this are twofold. One, since the CLEAr Lens is made from PMMA, it is not optically transparent, thus making imaging studies difficult. Two, the CLEAr lens has an array of 33 holes, each 400 µm diameter, drilled through it (see Figure 4A,B); these holes further challenge the ability to image through the lens. Taken in combination, the aforementioned reasons motivated us to design a CLEAr lens analog. This analog lens had to mimic the geometry and closely match the mechanical properties of the CLEAr Lens, while providing the important quality of optical clarity. Additionally, to allow for a precise measurement of the PoLTF, the inner surface (i.e. the surface contacting the cornea) of the analog lens had to be perfectly smooth and free mechanical imperfections. Any imperfections on the lens's inner surface can cause discomfort to the wearer and potentially lead to safety concerns such as a scratch cornea.

Confronted with these constraints, we first chose to construct the analog lens from the polymer polydimethylsiloxane (PDMS), and did so for the following reasons. PDMS is moldable; thus allowing us

to produce an analog that exactly matches the geometry of the CLEAr Lens. Second, PDMS is water-clear, which provides the sought after quality of optical transparency. Lastly, the stiffness of PDMS can be controlled by varying the ratio between polymer and cross-linking agent; this important property allowed us to produce a stiff lens from a moldable polymer. Specifically, we used Sylgard 184 (Dow Corning) at a 5:1 between polymer and curing agent.

To mimic the geometrical specification of the CLEAr Lens a two-piece mold was designed according to the CLEAr Lens specifications, and fabricated from aluminum (Figure 7)

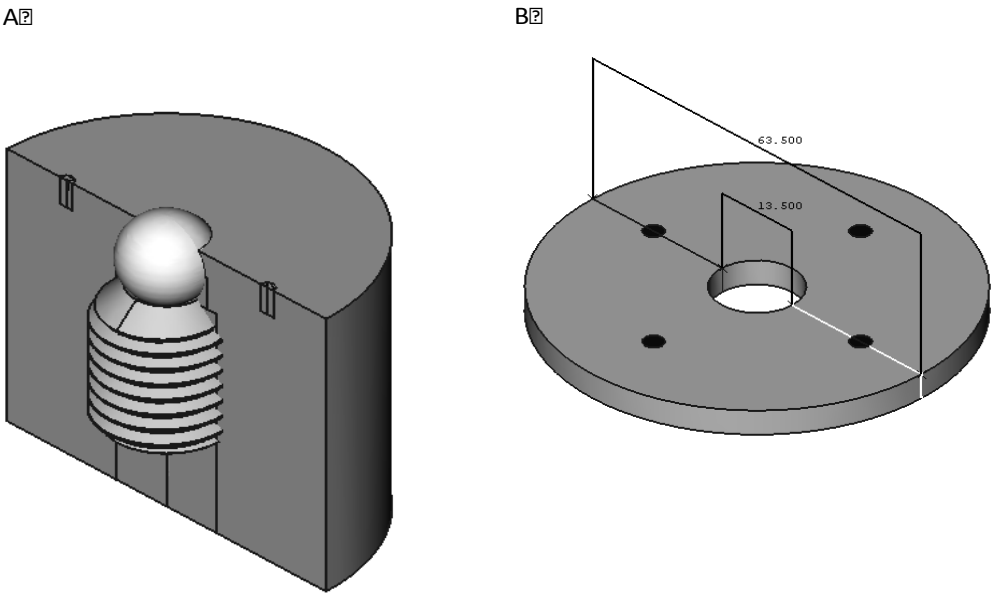

Figure 7: PDMS analog mold drawing. Both parts of the two-piece mold are illustrated above. Each cylindrical piece is 63.5 mm in diameter as shown by the large caliper in panel (B). (A) shows a cross-section of mold's base. A setscrew is used to press a stainless steel ball bearing into a spherically cut pocket; the bearing used had a radius of 7.541 mm and determined the radius of curvature of our contact lens. (B) shows the top part of the mold. When screwed to the base via the four radially symmetric holes, the center hole surrounds the bearing. This hole creates a void that is filled with PDMS to produce the lens (Due to poor contrast it is hard to read the measurement above this hole; it is 13.5 mm). Also, the base drawing should show a 3rd screw hole, which has been excluded from the above illustration.

The mold was then filled with PDMS mixture and the curing process was initiated. To cure the lenses, the filled mold was placed in a vacuum oven and baked at a temperature of 100°C for one hour. Subsequently, the mold was left to cool, and was allowed to finish curing overnight at room temperature.

Thereafter, the lenses were removed from the mold and inspected for defects. If no defects were noticeable, the lenses were cleaned and stored for later use. However, after fabrication, but before use, it

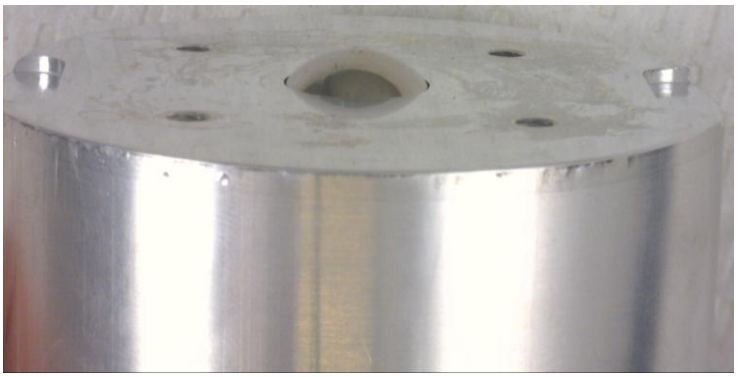

Figure 8. Base of PDMS Mold. Note how the bearing is protruded; this is what creates the curvature for our CLEAr Lens analog. Prior to filling a top piece is screwed onto the base creating a cylindrical void around the bearing that is filled with PDMS.

became apparent that the hydrophobicity PDMS would pose an experimental obstacle. Namely, hydrophobicity makes the PDMS lenses very unwettable and prone to adhesion to the cornea. This effect was not sought after, and methods to make the PDMS lenses more hydrophilic were explored. To this end we chose to plasma treat the lenses, a common method of reducing hydrophobicity (Owen and Smith, 1994).

As it turns out, however, our decision to use OCT instead of a flurometric imaging approach provided a certain degree of leeway in terms of the required optical clarity; even through turbid (i.e. cloudy) tissue, OCT remains a proficient imaging modality (Mao *et al.,* 2010). Furthermore, in an ocular setting, OCT has demonstrated an ability to acquire clinically viable images though cataracts (van Velthoven *et al.,* 2006). In light of these results, we chose to create second CLEAr Lens analog from PMMA, the same material as the actual CLEAr lens. The PMMA analog was made by the same machinist who produced the CLEAr Lens (Eric Schmidt, College of Engineering Machine Shop). Also it was produced according to the same geometrical specifications as the CLEAr Lens. However it contained no through-holes. Importantly, the PMMA analog allowed us to exactly match the material properties of the CLEAr Lens, and thus the

forthcoming tear film measurements were not affected by differences in stiffness or hydrophobicity. This afforded the PMMA analog with distinct advantages of the PDMS version.

4.3. Specific Aim II: Optical Coherence Tomography Measurement of Tear Film Thickness

To image the PoLTF layer beneath the CLEAr Lens analogs, we used a Visante anterior segment OCT (Carl Zeiss, Germany). To be consistent with the meERG recording protocol, the subject's right eye was anesthetized via 1-2 drops of 0.5% (vol/vol) proparacaine ophthalmic solution prior to lens insertion, however unlike the meERG protocol, the subject's pupil was not dilated. After the proparacaine had been instilled upon the subject's eye, the subject's corneal topography was mapped. Subsequently, the lens cup was filled with saline solution, and the lens was placed upon the cornea. Immediately following lens insertion acquisition of images began. Images were acquired at roughly 45-second intervals, over a time period of 20 minutes. Immediately following lens removal, the subject's corneal tomography was again mapped. The before and after corneal topographies were then compared to assess the degree which the CLEAr Lens analog had reshaped the cornea.

Measurement of the images for tear film thickness was conducted using ImageJ (National Institute of Health). For every image, we measured the thickness of tear film underneath the center of the lens. In addition to the center, we measured the tear film beneath the superior and inferior regions of the lens to assess the possibly of an asymmetric PoLTF. Once located, we took line scans of grey-scale pixel intensity orientated perpendicular to the lens's corneal surface. In doing so, we determined the thickness of the PoLTF by measuring the number of pixels between peaks. Four measurements were taken at each location and averaged. Subsequently, by scaling the pixel values to a physical unit of distance we recovered values for tear film thickness and plotted the results as a function of time.

We first conducted the above imaging protocol using a CLEAr Lens analog made from PDMS. However as discussed in the previous subsection, certain limitations were associated with the PDMS analog. Thus we repeated the OCT imaging protocol using the analog made from PMMA described above, and analyzed them exactly the same way as was done for the PDMS lens.

4.4. Specific Aim III: Multi-Electrode Electroretinogram Recording

4.4.1. *Contact Lens Electrode Arrays*

Custom made contact lens electrode arrays were fabricated specifically for the purpose of performing multi-electrode electroretinogram experiments. Contact lenses were machined from PMMA. The lenses were concave on the cornea side and planar on the opposite side. Bonded to the planar side was a clear, flexible parylene cable that contained an array of exposed platinum electrodes. Clear parylene was chosen as the cable substrate to maximize light transmission, and the electrodes were brought into electrical contact with the cornea via lens through-holes filled with conductive saline (see Figures 4A and B). To facilitate transmission of the corneal potentials to the recording amplifier, the platinum electrodes were joined by conductive traces that connected to a flexible printed circuit connector, which connects to the amplifier via a custom-made circuit board. This combination of lens and cable constitutes the CLEAr Lens apparatus. Additionally, electrode impedance analysis was also performed on a prepared lens. The impedance of each channel was typically measured to be within the range of 85-115 kΩ at 100 Hz, a value of less than 0.1% of the amplifier impedance

In preparation for experimental use, the CLEAr Lens was cleaned and sanitized with a diluted Liquinox solution and rinsed with deionized water. Subsequently, immediately prior to recordings, the through-holes of the CLEAr lens were filled with a sterile saline solution (CVS Pharmacy). After the filling procedure was complete, a 100 Hz sine wave was passed to the CLEAr lens and the output waveform was inspected for abnormal changes in impedance or gain. If no changes were apparent, the lens preparation procedure was said to be finished. However, due to occasional incomplete filling the CLEAr Lens through-holes, 1-3 channels, out of the 33 available, were typically absent from the recordings.

4.4.2: Human Subject Preparation

Before recordings, the subject's right eye was dark-adapted for 30 minutes. Following the dark-adaptation period, a series of three eye drops was applied to the subject's eye; this was performed under dim red

light, as not to disturb the subject's dark-adapted state. First, the cornea was anesthetized via 1-2 drops of 0.5% (vol/vol) proparacaine ophthalmic solution. Subsequently, the pupil was dilated using single drops of both 0.5% (vol/vol) phenylephrine HCL ophthalmic solution and 1% (vol/vol) tropicamide ophthalmic solution. Once the cornea was anesthetized and the pupil dilated, skin electrodes were attached to the subject to provide reference and ground electrodes. The reference electrode was attached to the subject's right temple and the ground electrode was placed upon the left check. With the skin electrodes attached, the CLEAr Lens was then placed upon the subject's right eye. Immediately following lens insertion, recordings began.

4.4.3. Recordings

For all experiments, light stimulation was provided via a custom-fabricated stimulus source consisted of a diffuse acrylic dome backlit by a xenon flash lamp. Additionally, the stimulus source included neutral density optical filters and diffusers to ensure uniform illumination. Light stimuli consisted of brief (<1ms) white flashes given at one-minute intervals. Bright, saturating flashes where chosen to increase the likelihood that all position on the retina responded maximally. The measured luminance was 191 scotopic candela seconds per square meter.

Each stimulus flash evoked an ERG response that was simultaneously recorded on up to 33 individual electrodes. This family of simultaneous waveforms constitutes a meERG response. The recording sessions began immediately after lens insertion and lasted 25 minutes. Over this period we collected one response every 60 seconds. The signals from individual electrodes were connected to separate input channels of a commercially made multi-channel amplifier (MEA60, Multi-Channel Systems). A custom-made interface board was used to route signals from lens to amplifier, and to better accommodate recording of ERG signals, the pass-band of the amplifier was modified to record from a spectrum of 1-3000 Hz. Differentially recorded signals were digitized at 5 kHz, digitally filtered (1-500 Hz), and stored for further analysis.

4.4.4. Analysis

4.4.4.1 Overview

The goal of this Thesis is to explore how lens settling and changes in PoLTF thickness impact the recording of meERG responses. We recorded a time-series of meERG responses over 25-minute window. Recordings began immediately after lens insertion and were obtained every minute thereafter. Following acquisition, the response data was analyzed for spatiotemporal changes that occurred across the set of sequential recordings (for the remainder of this Thesis *sequential recordings* will be referred to as *runs*). From the analysis to be described below, it is expected that an on-line method of monitoring the lens settling process during meERG recording sessions can be developed and implemented.

4.4.4.2. Noise Analysis

As previously eluded to, 1-3 channels were typically absent from all recorded runs due to incomplete filling. In addition, individual runs were often corrupted by noise. To identify the degree to which a given run was corrupted by noise, the root mean square (RMS) variance of the baseline waveforms was measured over a 40 ms window, with a right-hand time limit 20 ms before stimulus presentation. Prior analyzing the baseline noise, traces from all available electrodes were set to a common pre-stimulus baseline of 0 μV. The RMS noise values across all electrodes in a given run were then averaged, providing a mean RMS noise level for each run.

Further noise analysis was also performed. The above approach only factors into amount of noise that is correlated across all channels. This is a noteworthy deficit; in the case of meERG recording, the ability to separate correlated from uncorrelated noise is important. Through multi-electrode electroretinography, it is hypothesized that a map of locally distinct corneal potentials can be used to spatially assess retinal function. In this capacity, correlated noise does not introduce a major obstacle toward extracting meaningful information from an array of corneal potentials; correlated noise shifts the signals in a uniform manner across all the electrodes. Thus, even in the wake of correlated noise, potential differences across the electrodes can still be detected. However, in the presence of uncorrelated signal fluctuations, these

potential differences can become masked or distorted. To this end, we sought to quantify the amplitude of uncorrelated noise across families of waveforms. We accomplished this by using a *leave-one-out* averaging method, in which a 'modified average' is subtracted from the individual waveforms. This 'modified average' is the average of all the waveforms in the family *except* the one from which the average is being subtracted. In computing these *difference waveforms,* we were able to quantify the amplitude of uncorrelated noise present by computing their RMS voltage at baseline as described above.

Unlike conventional electroretinography, multi-electrode electroretinography relies upon spatial differences in corneal potentials to interpret spatial differences in retinal function. In this capacity, the data set as a whole is only as meaningful as the potential differences contained within it. Thus, according to the notion that differences between individual electrodes must rise above the noise level to be useful in this context, we chose to use the global variance of the measured a-wave amplitudes as a measure of signal strength. Variance was computed across all electrodes for every run. These values were subsequently averaged across runs to give a global measure variance. The resulting value was taken to be our meERG *signal strength.* By taking the ratio between signal strength and the uncorrelated noise amplitude squared, we computed the SNR for all available waveforms, and determined those having a SNR below 2.5 to be corrupted by noise. However, the corrupted recordings were not immediately removed from the following analysis, therefore allowing the lens settling process to be considered as a potential source of noise.

4.4.4.3 Determination of a- and b-wave Amplitudes

Using full-field light stimuli consisting of a brief white flash, the predominant features present in the ERG waveform are the a- and b-waves. Hence, the following analysis is focused upon the inspection of these features. The a-wave amplitude was determined by calculating the voltage deflection between the pre-stimulus baseline and the voltage measured at a predetermined time point of 7 ms after stimulus onset. This a-wave evaluation time was chosen to be prior to the a-wave peak in an effort to minimize post-receptor contributions. B-wave amplitudes were also evaluated at a pre-determined time point prior to the peak. This time point was chosen to be 29 ms after stimulus onset. Our rationalization for choosing a set

time point rather than the conventional method of using the trough-to-peak amplitude, was that the waveforms tended to drift substantially and unpredictably following the b-wave peak; some waveforms continued to rise well after majority of the waveform family had crested, thus some of the waveforms did not have a true b-wave peak. However, the voltage at this point alone was not taken to be the b-wave amplitude. To determine the b-wave's amplitude, we computed the absolute difference between our evaluated a-wave amplitude and the potential recorded at the b-wave evaluation time of 29 ms post stimulus.

4.4.4.4. Spatial Distribution of a- and b-Wave Amplitudes

To begin analyzing the distribution of corneal potentials, we examined the variance of a- and b-wave amplitudes across channels for each individual run. Electrical shunting through a thickened PoLTF was hypothesized to promote a meERG recording with less variance than the thin and settled PoLTF case, where the channels are thought to be more 'electrically independent'. This hypothesis was investigated by taking the standard deviation from the mean of both the a- and b-wave amplitudes, thus giving a single-number measure of the amplitude spread in a given run. The standard deviations were then compared across the runs, allowing amplitude dispersion to be viewed as a function of time.

However, in the realm of meERG data analysis, the standard deviation may not serve as the best way to evaluate the amplitude spread across runs. When taking the standard deviation from the mean, the differences are squared, creating a scenario in which data points lying far from the mean are weighed unevenly compared to the closer values. In this regard, we investigated the dispersion of amplitudes via an alternate method, a mean-difference approach. We computed the absolute potential differences between electrodes in a pair-wise manner and averaged them according to the following equation (modified from Lehmann and Skrandies, 1980),

$$Hilliness = \frac{1}{N-1} \sum_{i=1}^{N-1} \frac{\sum_{j=i+1}^{N} u_i - u_j}{i}_{(i \neq j)} \quad (1)$$

Where $u_{i,j}$ represents the voltage measured at each electrode, and N represents the number of available electrodes. The results of the mean difference analysis were then examined as a function of time. Also, the term *hilliness* in Eq. 1 was used to impart physical meaning to equation. A greater mean difference is associated with a more hill, or jagged, meERG response topography.

4.4.4.5. Spatiotemporal Trends of a-Wave amplitudes

Up to this point, we have only discussed global variance approaches to investigate for artifacts caused by a thickened tear film. In using this approach we overlooked multi-electrode electroretinography's primary purpose: to record spatially localized corneal potentials. In this regard, the global variance methods described above are limited and fail to provide localized insight. It was postulated that a thickened tear film might cause localized effects that are especially apparent under areas of the lens beneath which the PoLTF is the thickest. To peer into this possible effect, the a-wave amplitudes for each electrode were plotted as a function of time. Separate electrodes were plotted on offset traces, and to provide a spatial coordinate, the traces were grouped according to the ring in which the resided. An enlarged view of the electrode layout can be seen in Figure 9. Note how each ring has been assigned a letter, and the electrodes contained within that ring have been numbered increasingly in a clockwise direction. For the remainder of the Thesis, this convention will be used when referring to specific electrodes.

Once the amplitudes had been arranged in this manner, we analyzed the amplitude versus time traces for temporal trends and gained insight into how the meERG amplitudes change at the level of individual electrodes. Importantly we noted that some of the electrodes, primarily the periphery ones located on the A-ring, deviated significantly from the spatial mean (i.e. the mean of amplitudes across the electrode array). From this observation, we asked whether these significant deviations occur randomly across electrodes in the periphery, or if they occur more regularly in a specific region of the cornea.

4.4.4.6. Localized Analysis of Corneal Potentials

The previous inquiry was motivated by the notion that a locally thickened tear film would produce localized effects between nearby electrodes. To further explore this possibility we again used a mean-

difference approach. However, unlike the global approach described above, we divided the electrode array into five groups. One group consisted of the C-ring and middle electrode, and the remaining four groups were determined according to corneal quadrant (i.e. nasal, temporal, superior, or inferior; see Figure 9). Absolute potential differences were then computed and averaged amongst each group as described by Eq. 1. This approach provided us a more localized perspective of the cornea's electrical topography.

Our analysis methods thus far have relied heavily upon calculating some form of the cornea's average electrical topography, across either the entire electrode array or a certain subsections of it. Through averaging, we acquired insight as to how flat or jagged the topography was on *average*. In doing so we traded information on the level of single electrodes for information on the larger scale. This left us unable to determine the locations of peaks, valleys, or plateaus within the cornea's electrical landscape. In response, we decided *not* to average the pair-wise differences between a-wave amplitudes. Instead, we placed these differences into matrices that were organized according to electrode-electrode pair. Each matrix corresponded to a single run. These matrices can be thought of as *topographic signatures*; they numerically express the cornea's electrical topography at the resolution of single electrodes. Furthermore, when the topographic signatures for all runs are taken as a complete set, they can be used to provide temporal insight.

To begin our temporal analysis of topographic signatures we averaged them across time and computed a mean topographic signature. This was done for the entire time series and for the former and latter halves of the recording session. Importantly spatial information on the level of individual electrodes was left intact. From these mean topographic signatures we could see how the electrodes were related to one another and their relationship to the entire electrode population. Moreover, by averaging, the topographic signatures provided template representations of electrode behavior.

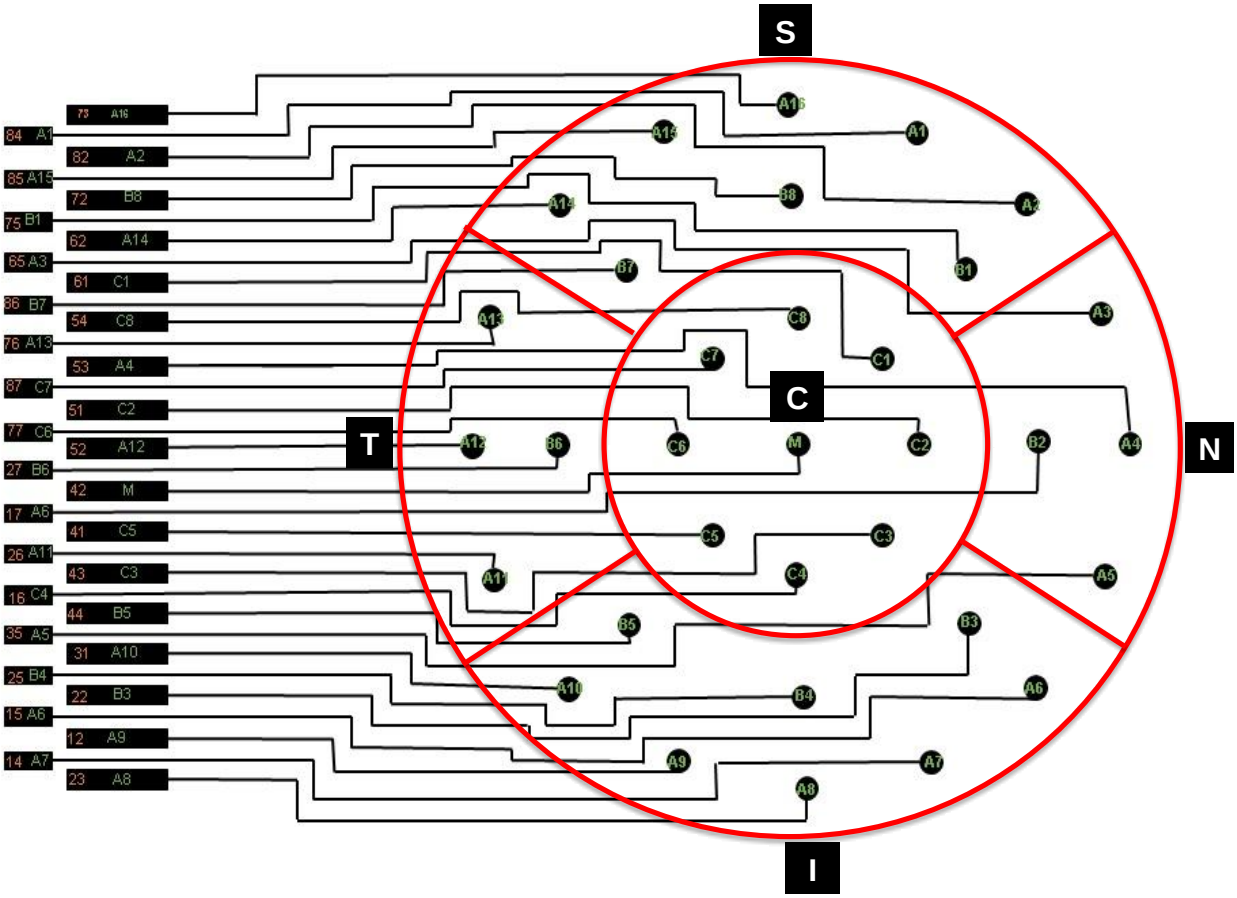

Figure 9: Electrode map of CLEAr Lens. The above figure shows how the electrodes on the CLEAr lens are named and grouped. The electrodes are grouped into three concentric rings (A,B,C) about a middle electrode (M). Also shown is the mapping from lens to amplifier; the red numbers are the corresponding channels on the multi-electrode array. Furthermore, we subdivided the array into 5 groups outlined in red above, and are referred to as S,N,I,T, and C which stand for superior, nasal, inferior, temporal, and central respectively. *Note: in the recording session electrodes A14, A16, and B8 were nonfunctional.*

4.4.4.7 Temporal Comparison of Multi-Electrode Electroretinogram Response Topographies

Early meERG work has yielded promising results that mapping of bioelectric potentials across the cornea is an indicator of retinal function. To function in this context, a stimulus that is nearly identical from trial-to-trial (such as the one used in these experiments) is expected to evoke similar meERG responses across successive trials. Accordingly, we probed the possibility that a thickened tear film, or the lens settling process, might be adversely affecting the ability of multi-electrode electroretinography to capture topographically similar potential maps across repeated trials.

To continue investigating spatiotemporal changes in electrical topography, we compared the mean topographic signatures from the former and latter halves of the recording session by computing the difference between them. In doing so, changes that occurred between the two halves of the recording session could be emphasized at the level of individual electrodes. While this approach could effectively inform us as to whether or not significant changes occurred between the two recording session halves, it provided no indication as to how the individual runs compared to one another.

In an attempt to ascertain this information, we quantitatively compared the cornea's electrical topography across individual trials. This was done via computing element-by-element absolute differences between all possible pair-wise combinations of topographic signatures. Each unique pair generated a *difference signature.* Taking each difference signature to be a sheet, we arranged them by run number, and generated a three dimensional array for each run. We now had an arrangement of 24^2 difference signatures. Via averaging all of them, we were able to assign every pair-wise combination of runs a *difference score* according to the following equation:

$$\boldsymbol{DS}_{k_1,k_2} = \frac{1}{N-1} \sum_{i=1}^{N-1} \frac{\sum_{j=i+1}^{N} \left| u_i - u_j \right|_{k_1} - \left| u_i - u_j \right|_{k_2}}{i}_{(i \neq j)} \quad (2)$$

In the above, the subscripted quantity, **DS**, is an element of the **D**ifference **S**core matrix and scores the difference two runs, k_1 and k_2. Note also how the subscripted differences, (u_i-u_j), are elements of the topographic signature as described above. However, in the spirit of keeping the notation similar to Eq. 1, a *difference-of -differences* approach has been emphasized. The elements of the difference score matrix are the average values of the difference matrices described above. We have essentially taken our 24^2 difference signatures, tiled them in a square pattern, and averaged each sheet, gives each 'tile' a number describing the degree of difference (of similarity) between all binary run combinations. Through such an approach, trends in meERG response repeatability can be visualized and used to guide further analysis.

4.4.4.8. Topographical Orientation Analysis

Operating under the hypothesis that a thickened tear film might cause signals across neighboring electrodes to be electrically shunted together, we decided to analyze the topographic signatures for pairs of electrodes with similar bioelectric potentials. This was done according to the notion that we could connect these pairs of similar potentials with lines that were indicative of 'average' equipotential lines, thus affording us a method investigate the orientation of the electrical topography evoked during meERG responses. We scanned the topographic signatures for values equal to or below 0.2 μV. The cutoff value of 0.2 μV corresponded to 2% of the global mean difference of a-wave amplitudes[4], and served to identify electrode pairs that are significantly more similar than would be predicted by the mean difference. We next counted the number for each run and examined how the number of counts changed as a function time. Additionally, we considered the spatial arrangement of these *level pairs* and how their arrangement changed as a function of time following lens insertion. Toward this end, we connected these level pairs with lines that approximated the average heading of equipotential lines.

The orientation of the lines connecting the (nearly) equipotential pairs provided a primitive means of investigating the cornea's *topographical orientation*. That is, by analyzing orientation of these connecting lines, we can get a grasp on the general direction the equipotential lines will follow. Equipotential lines are commonly used to map three-dimensional surface on a two-dimensional plane and are often drawn with the aide of interpolation. However no such interpolation was used here. We assumed that while interpolation would cause the equipotential lines to bend and curve around other topographic features present in our data set, it would not significantly alter their average heading. Moreover, an interpolated approach has been intentionally avoided in this situation. Interpolation algorithms are often computationally taxing and slow. Both are undesirable attributes should the meERG analysis techniques described here be adapted for use in on-line methods.

Through this approach we can acquire a sketch of how the cornea's electrical landscape is spatially orientated and how this orientation changes with time. To do so, we computed the angles of the lines

[4] The global mean difference was calculated in a similar way as the global variance, by averaging across space (electrodes) and time (runs).

connecting our equipotential electrode pairs. To focus upon the orientation of these lines (and not their direction) we constrained all angle measures to the range of 0 to 90 degrees, representing the nasal-temporal and superior-inferior axes by 0 and 90 degrees respectively. Should the orientation of the of the cornea's electrical landscape is radially uniform, the angles would be randomly distributed and not preferentially favor a particular axis. In this case the average angle would be 45 degrees. We examined our data such a preference by comparing the distribution of measured angles to one drawn randomly from a uniform distribution that also ranged 0 to 90 degrees.

4.4.4.9: Proposed On-line Method for Monitoring Multi-Electrode Electroretinogram Responses for Effects Associated With Tear Film Thickness

This project was designed to study the tear film dynamics underneath the CLEAr Lens during the lens settling process, and evaluate how changes in PoLTF thickness affect meERG responses recorded during the settling period. From this insight it is hoped that meERG responses can be monitored on-line for changes in responses occurring due to the lens settling process (or any other unwanted artifacts). This is perhaps the ultimate goal of the analysis explained above. To culminate these efforts, a computationally simple algorithm for analyzing recording quality is described below. We make no *a priori* assumptions about average topography, and compare the current run only to the previously collected ones. A block diagram summary of our algorithm is given in Figure 10. There remains a good deal of flexibility in terms of refining the algorithm, and many methods exist for weighting the differences with previous runs.

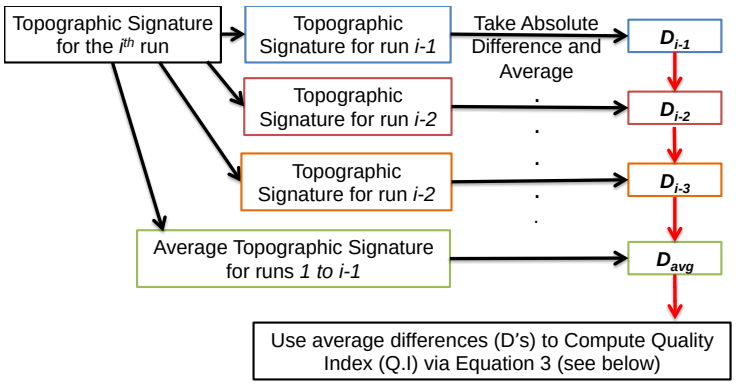

Figure 10: Recording quality algorithm block diagram.

In our algorithm, we evoke the use of topographic signatures to compare runs against one another. Doing so, we make use four different topographic signatures. One is the topographic signature of the most recent, or i^{th} run. The remaining three are subtracted from that of the most recent run, these include a topographic signature of run *i-1*, a topographic signature of run *i-2*; and a *running average* topographic signature, which averages topographic signatures *1* through *i-1*. Upon computing what equates to the aforementioned difference matrices, we took the absolute value of each element and averaged the differences. This essentially gave us three difference scores, D_{i-1}, D_{i-2}, and D_{avg}, from which we computed a recording *quality index,* QI using the following equation[5].

$$Q.I. = \frac{1}{D_{avg}} + \frac{1}{D_{i-1}} + \frac{1}{4D_{i-2}} + \frac{1}{9D_{i-3}} \quad (3)$$

According to Eq. 3, runs received a higher QI score if they were similar to the running average and the two previous runs. This approach can be viewed as a cumulative moving average method that places particular emphasis on the three most recent runs. The recent runs are given more weight than the average to account for large changes in the average than occur during the first several runs, and serve to make our method viable even in the early runs. Such an attribute is especially beneficial given that a normative meERG data set has not been established. Thus a mean, template response from healthy individuals does not yet exist either. In this regard, we have designed the above method to evaluate the quality of a given sequentially recorded runs run without the aid of a mean response.

[5]We did not calculate a quality index for the first two runs. And when calculating for the third run, the rightmost term in Equation 3 is omitted.

5. RESULTS

5.1. Specific Aim I: CLEAr Lens Analog Results

The PDMS CLEAr Lens analog was designed and made to closely resemble the actual CLEAr Lens while provided the optical clarity necessary to image through. From the standpoint of optical clarity, the lens performed well. However, due to slight differences in geometric specifications, and vast differences in material properties, the PDMS CLEAr Lens failed to serve as a viable analog through which to replicate the CLEAr Lens scenario.

In terms of material properties, PDMS and PMMA each possess significantly different measures of hydrophobicity and stiffness. Left untreated, PDMS is far more hydrophobic than PMMA. The very hydrophobic nature of PDMS instituted concerns that a contact lens made from such a material might adhere strongly to the cornea, and possibly cause damage upon removal. To lessen this risk, we plasma treated the PDMS lenses as a means of reducing the hydrophobicity, and verified the effectiveness of the plasma treatment by measuring the hydrophobicity via contact angle meter before and after treatment. Additionally, the hydrophobicity of the PMMA CLEAr Lens was evaluated; results for the three materials are shown in below.

TABLE I
HYDROPHOBICITY OF LENS MATERIALS

Material	PMMA	PDMS (Untreated)	PDMS (Plasma Treated)
Contact Angle (Degrees)	108	141	69

Plasma treatment of PDMS cut the contact angle in half, indicating that the hydrophobicity of the lens had decreased considerably. However, the decreased value was found to be further from that of PMMA. Despite this increased difference from CLEAr Lens material properties, we chose to plasma treat the PDMS due to safety concerns regarding the very hydrophobic nature of untreated PDMS.

The PDMS lenses were also found to contain slight geometrical differences compared to the rigid CLEAr Lens. Most notably, we enlarged the diameter of PDMS lens to 13.5 mm compared to the 12.5 mm diameter of the CLEAr Lens. This was done to provide support for the PDMS while curing and aid in removal from the mold. Also, the PDMS analog had sharper edges than the PMMA lens. As a result of the polishing process that is performed on the PMMA lenses, the edges become softened. This effect was not replicated on our PDMS analog lens because the CLEAr Lens drawings used to design our PDMS mold indicated a sharp edge. These differences between CLEAr Lens analog and the actual CLEAr Lens prevented the PDMS lens from serving as a viable alternative for imaging experiments. In light of the differences between the PDMS analog and the CLEAr Lens, we decided to produce another analog from PMMA. Even though this analog had identical material properties to those of the CLEAr Lens itself, slight differences remained. Again the analog had no through holes, and differences in machining produced slight difference between the CLEAr Lens and its analogs.

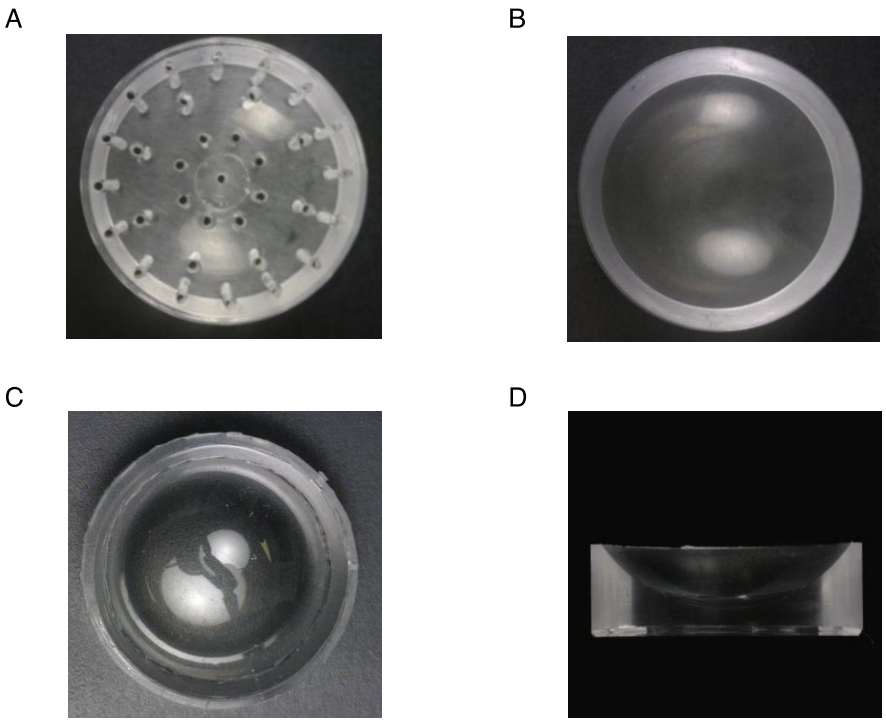

Figure 11. Pictures of CLEAr Lens and CLEAr Lens analogs. (A) shows an image of the actual CLEAr Lens, 'cup' side up, with no cable attached. (B) shows the PMMA CLEAr Lens analog. As in (A), the lens cup is facing up. (C) shows the PDMS analog, again with the lens cup facing up. (D) shows a cross section of the PDMS analog; note the sharp edge and wide lip.

5.2. Specific Aim II: Optical Coherence Tomography Measurement of Tear Film Thickness

A Visante anterior segment OCT was used to image the PoLTF and measure its thickness. The imaging sessions began within ~30 seconds following the insertion of a CLEAr Lens analog and lasted 20 minutes, over which time images were obtained at roughly 45 second intervals.

5.2.1. Imaging Through a PDMS CLEAr Lens Analog

Initially, the imaging experiments were performed using a PDMS analog. A representative OCT image showing he PoLTF beneath the PDMS analog is shown in Figure 12.

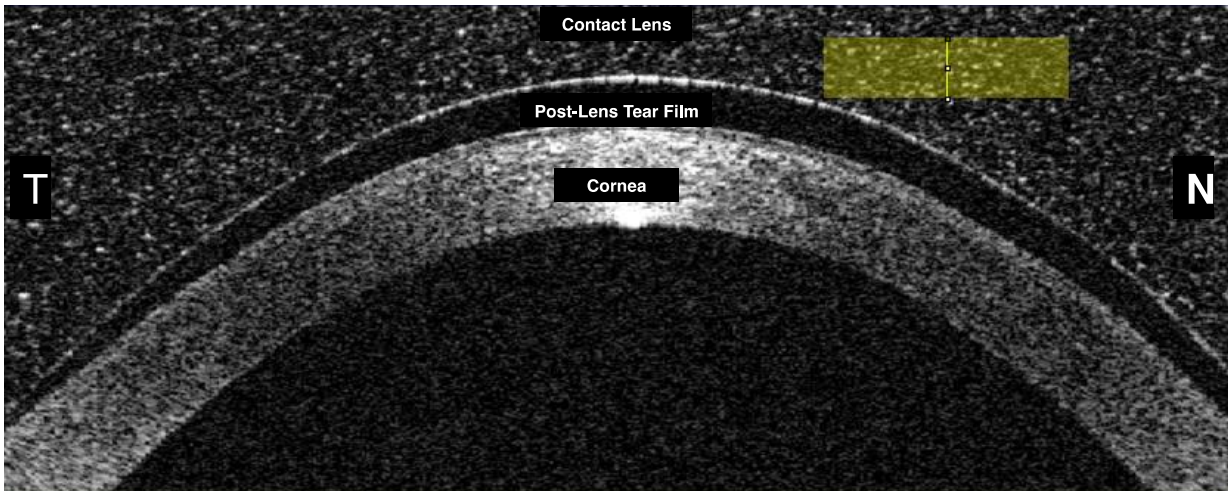

Figure 12. OCT image of tear film beneath PDMS analog lens. Pictured above is an image of the PoLTF along the nasal-temporal axis (indicated by the N and T above). The height of the scale bar; is 493 μm. Distance scaling shown in this unusual fashion to allow the Figure's viewer to 'mentally slide' the bar atop the tear film with ease.

The time-series of OCT images were measured for PoLTF thickness. We performed these measurements by taking intensity line scans perpendicular to the lens-PoLTF and PoLTF cornea interfaces, and computing the pixel distance between intensity peaks. An example line scan showing our measurement technique is shown provided in Figure 13. Pixel values were then converted to units of μm, and the PoLTF plotted as a function of time (Figure 14).

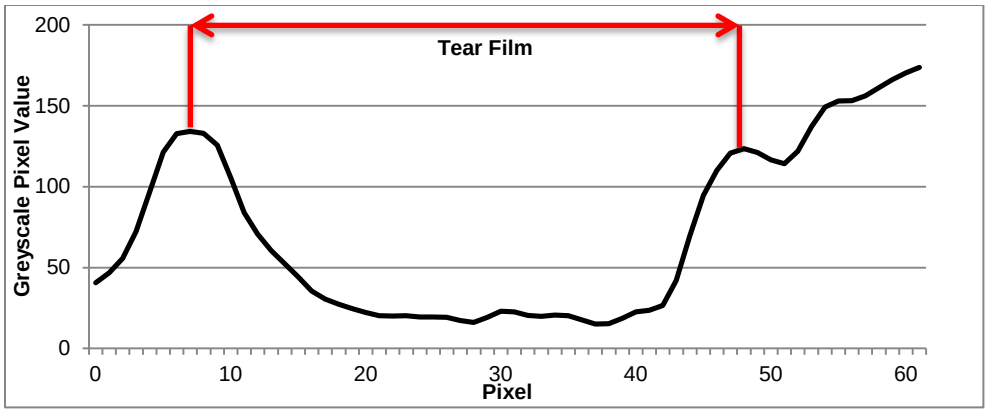

Figure 13. Line scan analysis example. A sample line scan of tear film thickness is shown above. Initially we measured this thickness in pixels (as shown on the horizontal axis) and later converted this value to um.

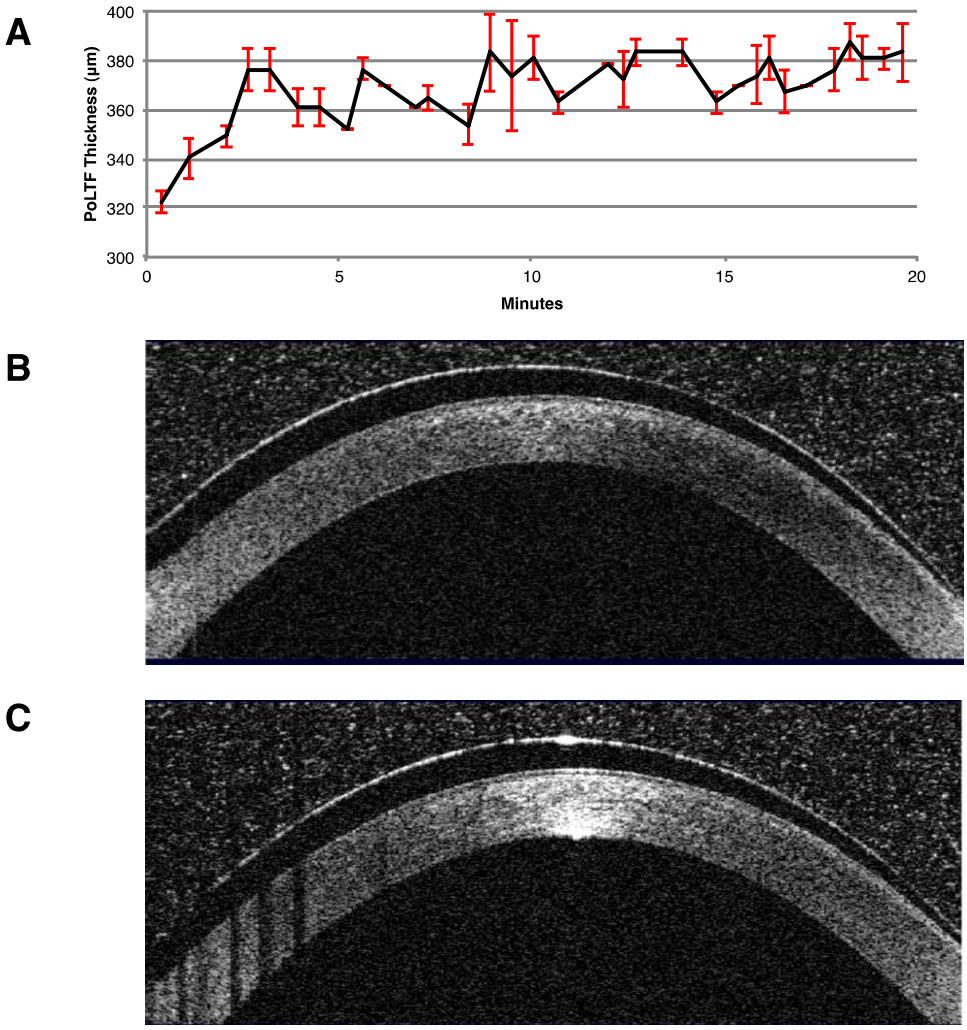

Figure 14: Tear film thickness beneath PDMS analog as a function of time. (A) PoLTF thickness is plotted as a function of time. Error bars represent the standard deviation from the mean. (B) An OCT image of the PoLTF acquired 2.5 minutes after lens insertion. (C) An OCT image nearly 20 minutes after lens insertion. Note how the central thicknesses are quite similar as predicted by (A). Also, the images in (B) and (C) were acquired about the superior-inferior axis.

The thickness of PoLTF measured underneath the PDMS CLEAr lens analog was much thicker than expected. Furthermore it did not thin as a function of time. Reasons for this surprisingly thick PoLTF will be explored in the Discussion. Though, one potentially useful observation did come of the PDMS analog imaging experiments. Cross-sections orientated along the superior-inferior axis showed a PoLTF that was a notably thicker beneath the inferior side of the lens. We measured this asymmetry in PoLTF thickness for eight images, the results of which are displayed in Table II.

TABLE II
SUPERIOR-INFERIOR TEAR FILM THICKNESS ASYMMETRY, PDMS ANALOG

Corneal Location of Measurement	Superior	Inferior	Central
Post Lens Tear Film Thickness (μm)	247.1	433.8	369.2
Measurement Error (± μm)	34.1	14.4	14.3

5.2.2. Imaging Through a PMMA CLEAr Lens Analog

In light of the above results, we chose to revise our methods, and chose to repeat the OCT imaging experiments using a PMMA CLEAr Lens analog. Again, even with a PMMA lens, we did not see a notable decrease of PoLTF thickness over time, and actually observed the PoLTF to become slightly thicker over the first few minutes following insertion (Figure 15). A representative image of the tear film beneath the PMMA lens is shown in Figure 16.

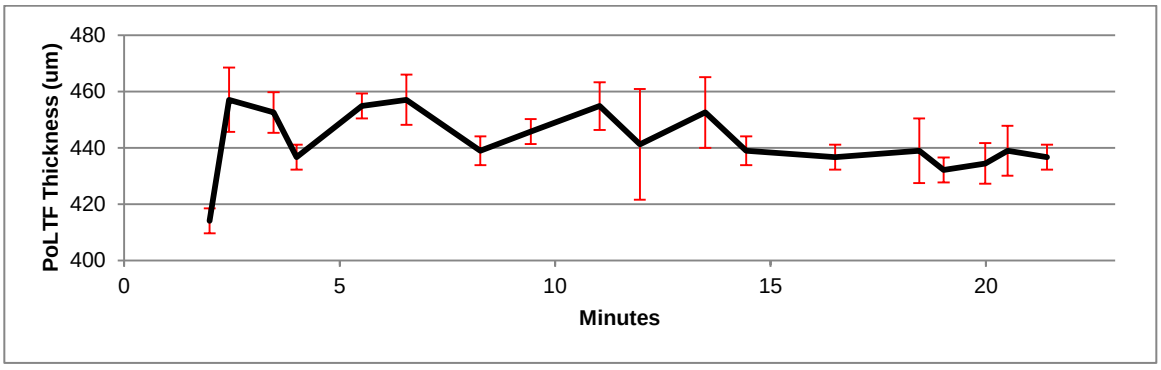

Figure 15. Tear film thickness beneath PMMA analog. Shown above is the tear film thickness beneath the PMMA analog. Red error bars denote +/- one standard deviation from the mean.

However, the superior-inferior asymmetry of PoLTF thickness was again present and very noticeable (see Figure 16). Thus we again measured the images (N=3) for this asymmetry (Table III). However, since only three of the 24 images acquired imaging through the PMMA analog were orientated about the superior-inferior axis, more imaging experiments are encouraged to verify this trend.

TABLE III
SUPERIOR-INFERIOR TEAR FILM THICKNESS ASYMMETRY, PMMA ANALOG

Corneal Location of Measurement	**Superior**	**Inferior**	**Central**
Post Lens Tear Film Thickness (µm)	174.0	485.7	454.6
Measurement Error (± µm)	27.1	28.3	10.9

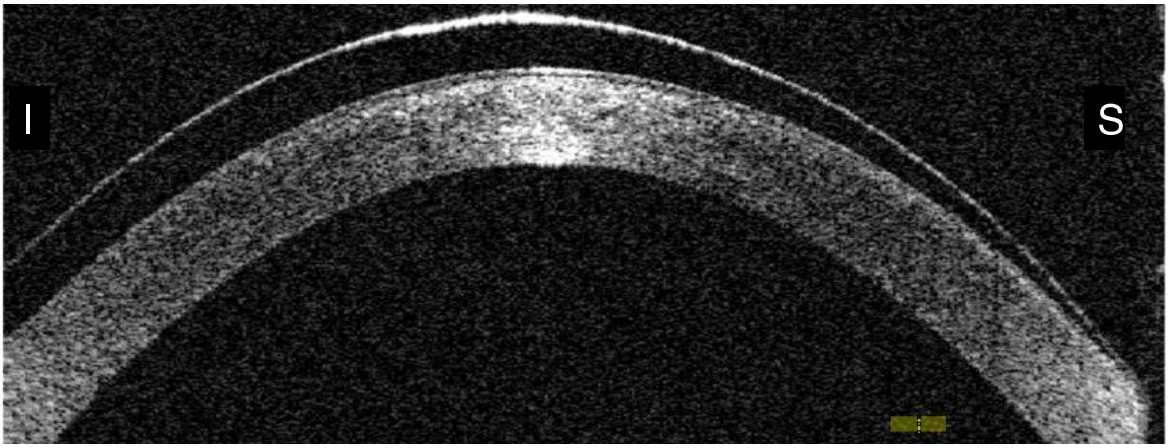

Figure 16. Tear film image through PMMA analog. Scale bar is 488 um long. This cross-section was acquired along the superior-inferior axis (denoted by S and I above). Note how the PoLTF is much thicker underneath the inferior half of the lens.

Aside from tear film thickness, OCT also provided an opportunity to investigate lens positioning. From Figure 16, it can be seen that the center of the lens is positioned toward inferior hemisphere of the cornea. Such off-center positioning may aid in explaining the superior-inferior PoLTF thickness asymmetry. A possible explanation for this positioning is a net downward force exerted by the eyelids. Photographs of the lens on the eye acquired with every OCT image support his notion, and show the lower eyelid being stretched downward by the lens (Figure 17). This is potentially result of force from the upper eyelid.

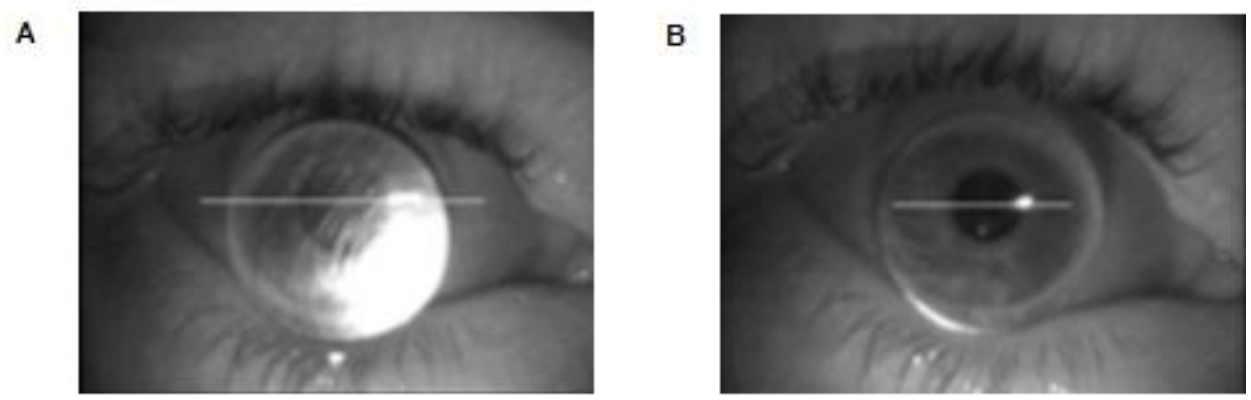

Figure 17. Positioning of PMMA analog on the eye. (A) Positioning of lens after ~2.5 minutes of wear. (B) Positioning of lens following ~20 minutes of wear.

Thus, while we were not able to observe a thinning of the PoLTF thinning as we had expected, the OCT imaging experiments still allowed use to ascertain insights that should be beneficial to the meERG project. These insights will be expanded upon in the subsequent chapter.

5.2.3. Corneal Topography Changes Due to Lens Wear

Before and after each imaging session (PDMS and PMMA) corneal topography was mapped to assess the degree to which our contact lenses reshaped the cornea. Additionally, we attempted to map the corneal topography after the meERG recording session, but did not obtain reliable measurements. With the before and after lens wear topographies, we were able to make difference maps to highlight corneal reshaping (Figure 18). For both the PDMS and PMMA analogs, the cornea was reshaped in both the superior and inferior quadrants, steepening its radius of curvature by about 5 diopters (or 0.8 mm) (Figure 18C and D). Via measuring corneal topography we could also measure the radius of curvature of the subjects eye and compare it to that of the lens. This was done before each imaging session and yielded measurements of 7.69 and 7.71 mm. These measurements indicate that subject's cornea was slightly flatter than the lenses which both had a radius of curvature of 7.54 mm.

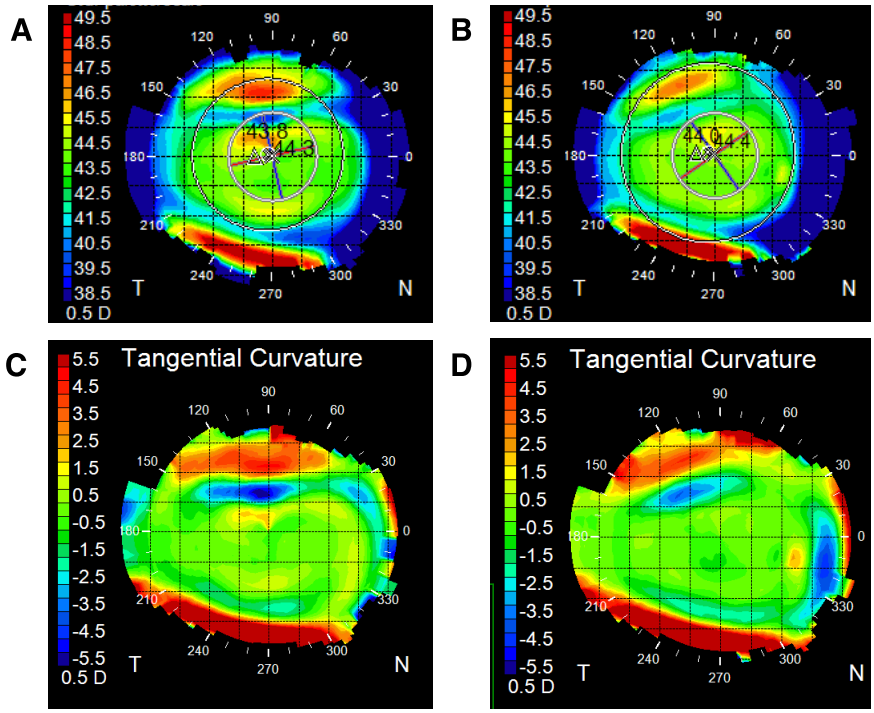

Figure 18. Lens induced changes In corneal topography. (A) shows the corneal topography *after* PDMS analog wear. (B) shows the corneal topography *after* PMMA analog lens wear. (C) shows the difference between (A) and the topography before lens wear. The dark reds are in both the superior (upper) and inferior (lower) quadrants and indicate that these areas of the cornea became slightly reshaped. (D) shows the same effect as (C) but for the case of the PMMA lens.

5.3. Specific Aim III: Multi-Electrode Electroretinogram Response Results

To evaluate the impact of tear film changes due to lens settling we began recording meERG responses immediately following lens insertion, and continued recording until we had a time series of responses spanning 25 minutes. We conducted two recording sessions, however, do to equipment malfunction, only one of the sessions produced reliable data. The reliably recorded session consisted of 24 runs spaced one minute apart. We did not obtain 25 runs (as the one minute spacing would dictate) due to a recording system error that prevented one of the runs from being properly stored for further analysis. This occurred one-minute after lens insertion, between recorded runs 1 and 2; unlike the remaining runs, these runs are spaced since two minutes apart. Care will be taken to emphasize this distinction in the forthcoming figures. The following results describe how meERG signals change in both space and time. Through the subsequent analysis, we hope to gain insight as to how the lens settling process might be affecting meERG recordings.

5.3.1: Noise in Multi-Electrode Electroretinogram Responses

As a starting point, we performed noise analysis to determine a typical SNR for our waveforms. To do so we evaluated the RMS voltage of the pre-stimulus baseline waveforms. The RMS values estimated the amplitude of noise across all frequencies contained within the recording system's bandwidth. After calculating the RMS voltages, we averaged them across the electrodes for each run; this provided a mean measure of the noise, at baseline, for a given run. Such noise analysis was insufficient and failed to separate correlated from uncorrelated noise. Through the separation of correlated and uncorrelated noise, we can determine relative contributions of each type of noise. Furthermore, knowledge of the noise's type provides information about its source. Correlated noise is largely biological, stemming from heartbeats, blink attempts, and other biological processes. Uncorrelated noise, on the other hand, is generated from within the recording system.

To determine the amount of uncorrelated noise present in the signals we used a *leave-one-out* average subtraction technique to produce *difference waveforms* that consisted only of uncorrelated noise. We then evaluated their RMS voltage at baseline and compared it to the correlated noise level (Figure 19A). By squaring these RMS amplitudes, we were able to estimate the noise power of both the correlated and uncorrelated noise (Figure 19B), and determine the percent contribution of each type (Figure 19C).

From Figure 19 we can observe that the total noise levels across runs fluctuate within well-defined range throughout the time-series and peaks at 10-minute mark. The uncorrelated levels also fluctuate in time, and interestingly, the uncorrelated noise level also reaches a maximum value at the 10-minute mark. Next we sought to find our out the uncorrelated noise is distributed across the individual channels, and how this might affect signal quality. To this end, we determined an acceptable SNR and used it to identify noise-corrupted recordings. We computed the SNR for all available electrode/run combinations, and displayed the results used a heat map (Figure 20A).

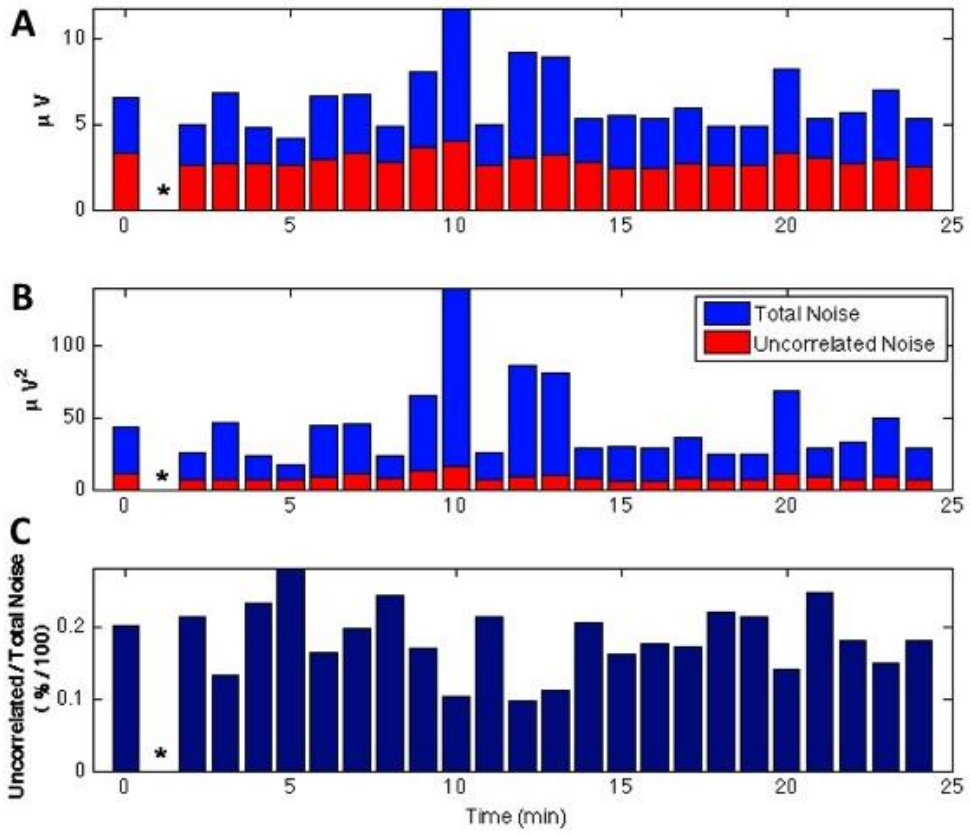

Figure 19. Noise analysis comparing correlated and uncorrelated noise levels. (A) RMS noise amplitudes are shown as a function of CLEAr Lens wear time. The height of the blue bars indicates the RMS amplitude of the total noise, while the red bars show the amplitude of uncorrelated noise. (B) Estimated power of both total (blue) and uncorrelated (red) noise. (C) Percent of total noise that is uncorrelated. Note, the asterisk present on all three panels represents the failed recording attempt occurring at the one-minute mark.

From the heat map alone the values below our criterion SNR level of 2.5 were difficult to see. To remedy this problem we colored the electrode/run pairs that failed to exceed this level fuchsia and redisplayed the heat map to highlight them (Figure 20B). It is clear from Figure 20 that electrodes in the A-ring generally have lower SNRs than do electrodes in the B and C-rings. And, more interestingly, on the 'noisy' A-ring electrodes, the inferior electrodes appear to be significantly noisier than those in superior region of the lens. This suggests that noise level might be influenced by position on the CLEAr Lens, and could therefore be linked to differences in tear film thickness under different lens regions as shown in Section 5.2. Thus we sought to better comprehend what might be occurring between the CLEAr Lens and corneal surface that would cause an apparent spike in noisiness. This prompted us to leave the noise-corrupted runs in our recording sets for subsequent analysis.

5.3.2. Spatial Distribution of a- and b-Wave Amplitudes

Does a thickened tear film cause the a- and b-wave amplitudes to become electrically shunted together? Our first approach toward investigating this question was to examine the spatial distribution of a- and b-wave amplitudes. A representative meERG waveform family is shown in Figure 21, and includes a magnified view of a-wave depression to illustrate that we do indeed have a distribution of amplitudes as opposed to a singular value.

A

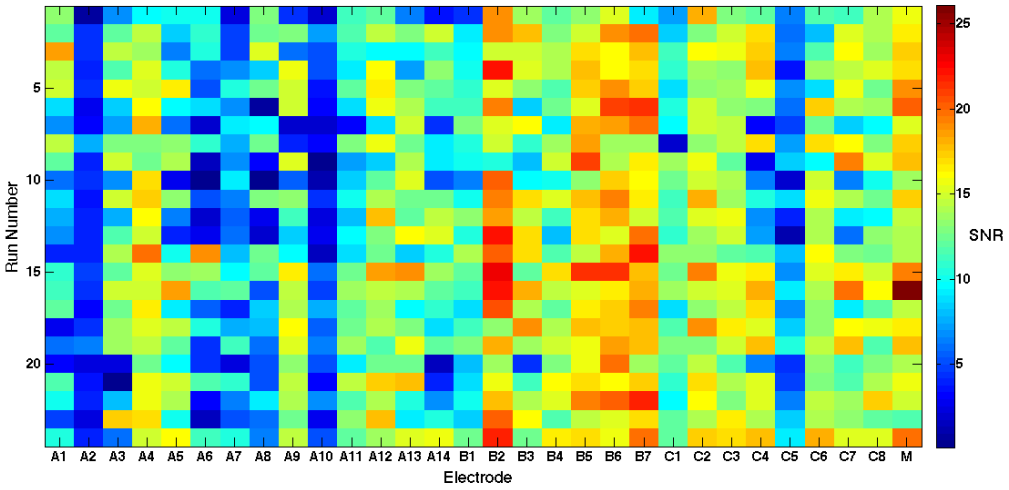

B

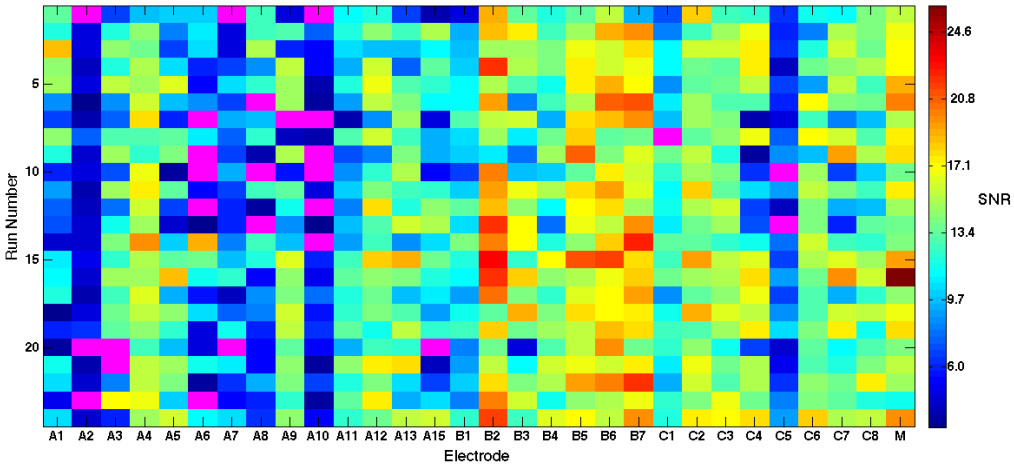

Figure 20. Signal-to-noise ratio heat maps. (A) shows a how the SNR varies across both runs and electrode. (B) Displays same information as (A) but with unacceptably low SNR values highlighted in fuchsia.

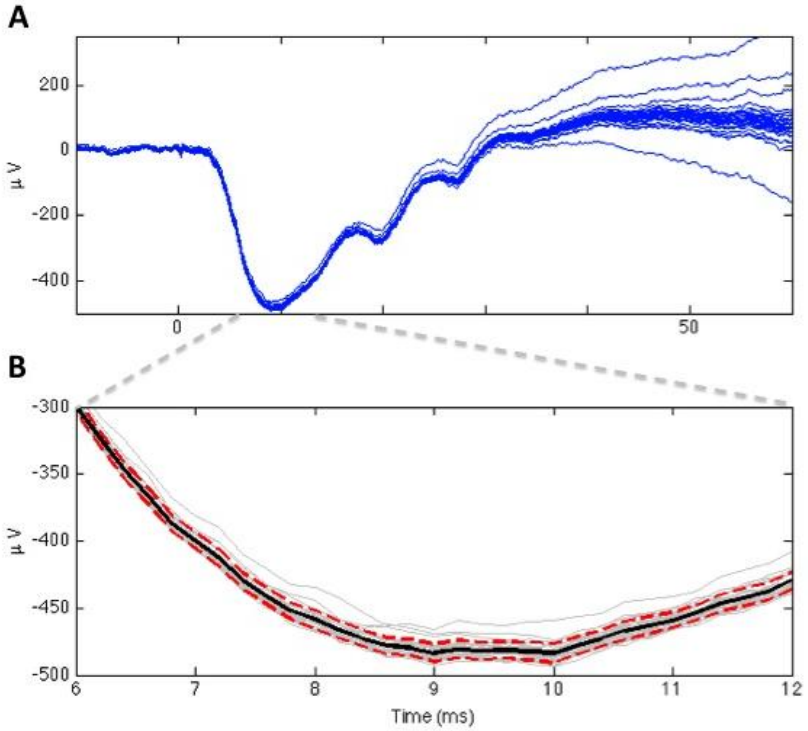

Figure 21. Example waveform plot showing distribution of amplitudes. (A) The blue traces show an example family of waveforms from 10 ms before stimulus delivery and 60 ms afterwards. (B) shows a magnification of the a-wave depression. The grey traces are the same as the blue above; the thick black trace is the average of all individual traces; and the dashed red lines bound the average by +/- one standard deviation.

We performed spatial amplitude distribution analysis across all available electrodes, and produced single-value quantities of amplitude spread for every run. This allowed amplitude distribution to be investigated as a function of time and was done by two complimentary methods. First, we calculated the standard deviation from the mean of the a- and b-wave amplitudes and plotted the results as a function of time (Figure 22). To compliment this approach we analyzed the spatial distribution of a- and b-wave amplitudes by an alternate method as described by Eq. 1 in the Methods section. Using this a mean-difference approach we acquired similar results and demonstrated the similarity by placing results from the complimentary approaches side by side (Figure 23).

According to our hypothesis, if the PoLTF does indeed change as a function of time the spatial amplitude distribution should as well. This notion was probed by statistically comparing spatial amplitude distributions for first and second halves of the recording session via Welch's t-test; the results of the are shown in Table IV.

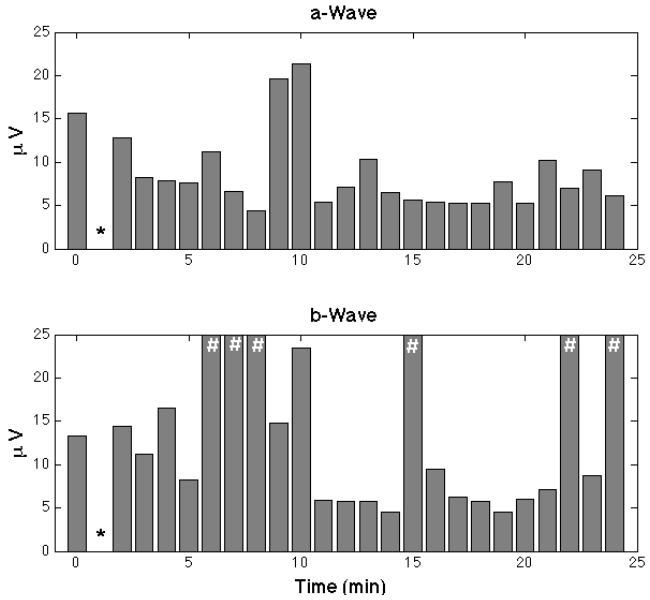

Figure 22. Using standard deviation to assess spatial distribution as a function of time. (A) shows the standard deviation of a-wave amplitudes from the mean. (B) shows the standard deviation of b-wave from the mean. The pound signs on top of the bars indicate that values that exceeded the axes. The asterisks represent the failed recording at the 1-minute mark.

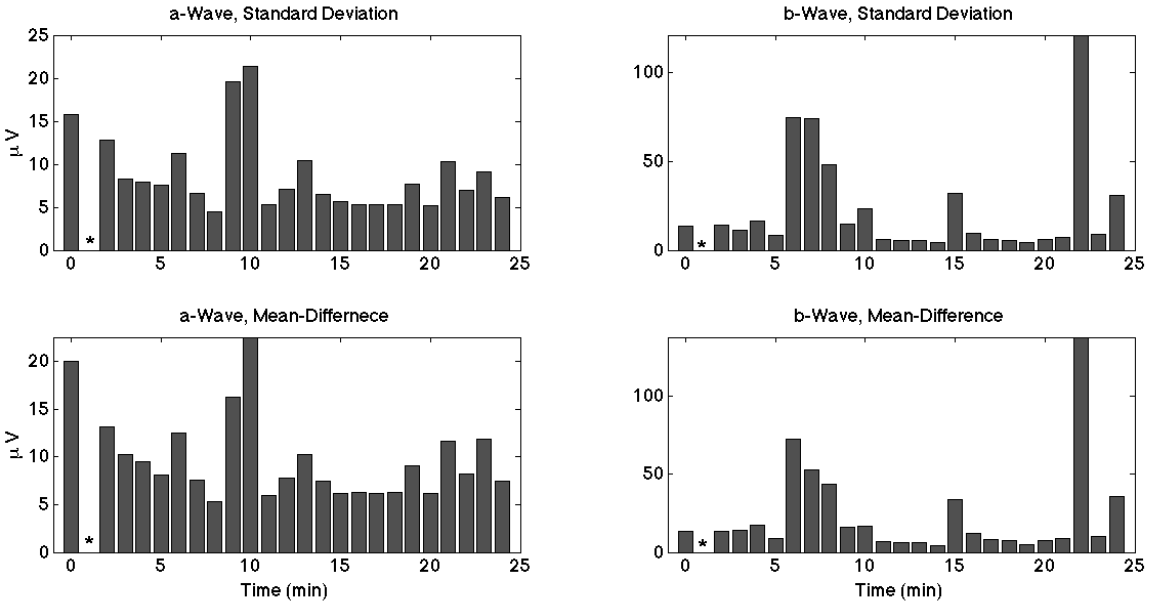

Figure 23. Comparing standard deviation and mean difference approaches for calculating spatial distribution. Results from the two complimentary methods are shown above. Again, the asterisk indicates the failed run. The difference scales between the a- and b- wave distributions plots was intentionally done to indicated that b-wave amplitudes exhibit far greater levels of distribution that do the a-wave amplitudes.

TABLE IV
P-VALUES ILLUSTRATE DIFFERENT A-WAVE AMPLITUDE DISTRIBUTIONS OVER FIRST AND SECOND HALVES OF THE RECORDING SESSION

	Standard Deviation Approach	Mean Difference Approach
a-Wave	0.049	0.060
b-Wave	0.642	0.974

From Table IV, it is clear that the first and second halves of the recording session produced statistically different a-wave amplitude distributions (i.e. $P<0.1$)[6], providing evidence that spatial distribution of a-wave amplitudes decreased as a function of time. The statistical analysis above indicated no such trend for the b-wave amplitudes. However, the b-wave amplitude distribution was abnormally high at the 23-minute mark (see Figure 23, right column), and could potentially be skewing the statistics. Moreover, the b-wave amplitudes exhibited greater variability than did the a-wave amplitudes (compare the axes across columns on Figure 23). This was exemplified by taking the mean of both the a- and b-wave spatial amplitude distribution values, which for the a-wave and b-wave 9.82±4.46 μV (mean ± S.E.M) and 23.3±29.7 μV respectively. In light of the high variability of b-wave distributions (the S.E.M is greater than the mean), we chose to conduct the remaining analysis using only a-wave amplitudes.

5.3.3. Spatiotemporal Trends in a-Wave Amplitudes

How do the a-wave amplitudes themselves change as a function of time? In asking this question, we sought to examine the possibility that the amplitudes themselves (not the spatial distribution) changed as a function of time. Initially, we averaged the a-wave amplitudes across the electrode array for every run and subsequently plotted these average values as a function of time (Figure 24).

Next we asked how the spatial distribution of a-wave amplitudes, at the resolution of individual electrodes, changes as function of time. Accordingly, we plotted a-wave amplitudes for each electrode as a function of time and spatially separated them by offsetting the traces (Figures 25). Even before continuing with quantitative analysis, it can be seen that the A-Ring electrodes show considerably more amplitude

[6] The cutoff P-value of 0.1 is higher than the typical value of 0.05, and was made based upon our limited sample size.

variation that do those on the B- and C-Rings. This effect appeared especially pronounced on electrodes A6-10, all of which were inferior electrodes, and indicated that distribution of a-wave amplitudes might by vary predictably across space.

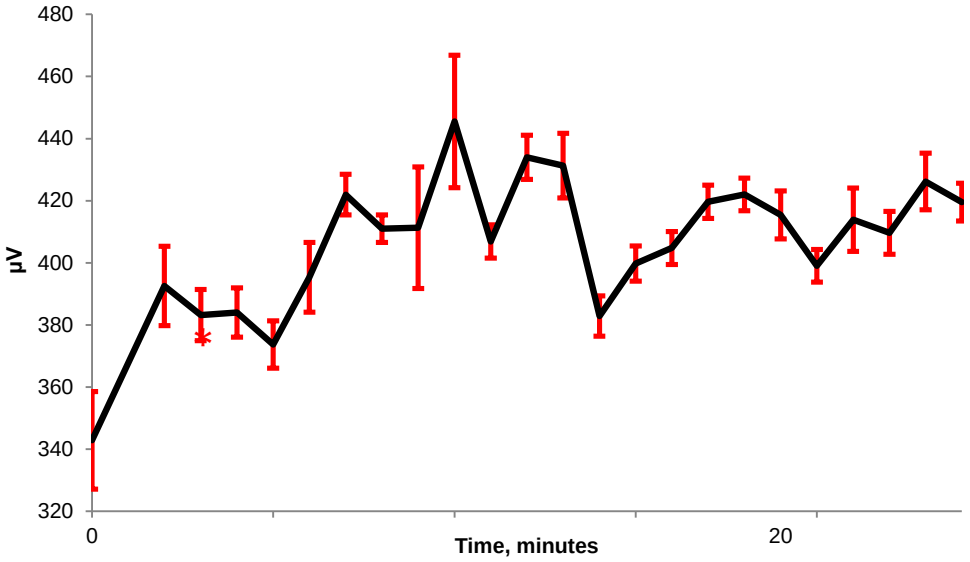

Figure 24:Time course of average a-wave amplitudes. The above plot displays a-wave amplitudes as a function of time and the error bars show +/- one standard deviation from the mean. The asterisk in place of the error bars denotes the failed run at the one minute mark.

5.3.4. Localized Distribution of Corneal Potentials

Does amplitude distribution depend on spatial location? To probe this inquiry, we subdivided the electrodes array into groups of electrodes, and computed the amplitude distribution within each group using the mean-difference approach (Eq. 1). It was natural to divide the A and B rings of the electrode array into quadrants, while grouping the C-ring and middle electrode into one central cluster, thus yielding five regions for analysis. Figure 26 shows the spatial distribution of a-wave amplitudes for the five regions described above.

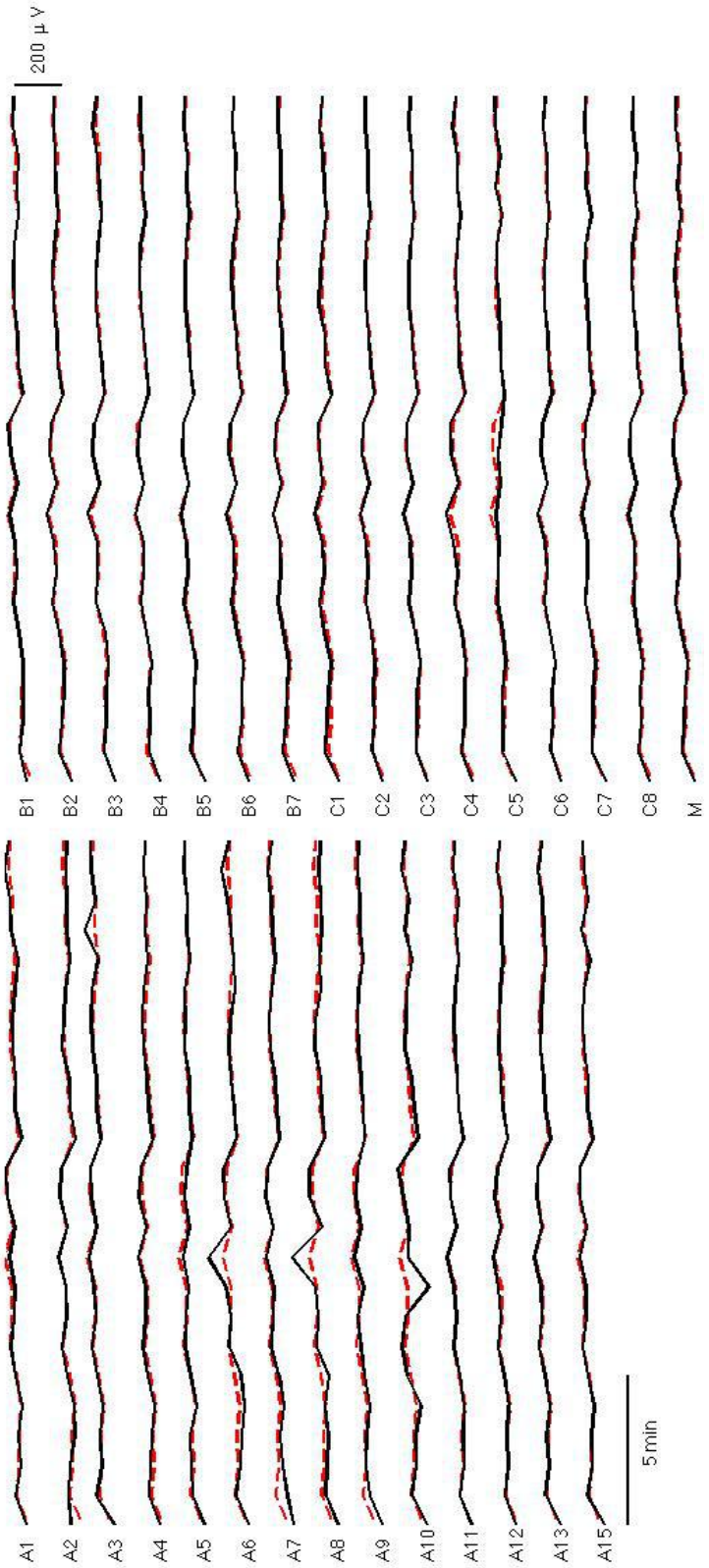

Figure 25: a-Wave amplitudes plotted as a function of time for individual electrodes. The black lines show the amplitudes for each electrode. These black traces are plotted a top red dashed lines that denote the time course of the average a-wave values as shown previously in Figure 24.

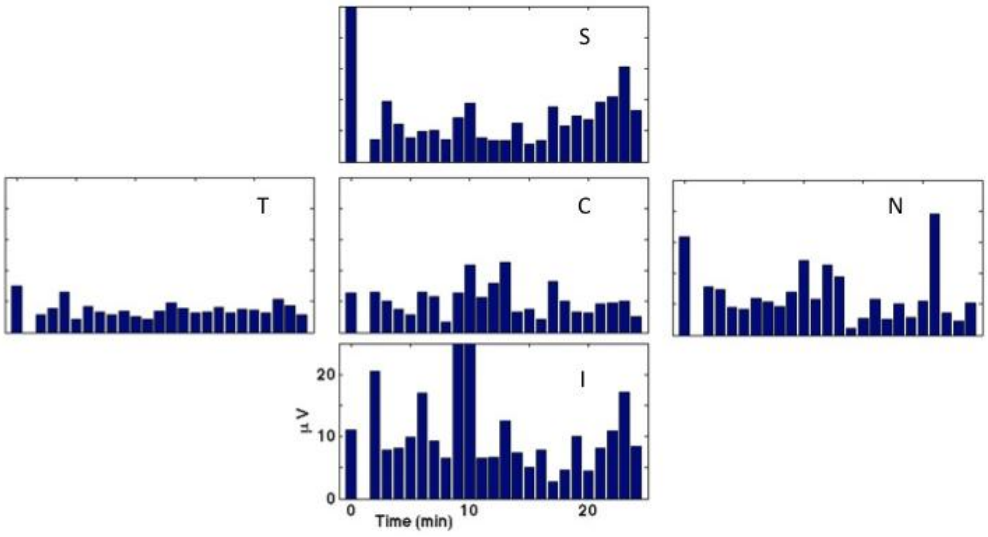

Figure 26. Spatial distribution of amplitudes vary across the cornea. The plots show amplitude distribution as a function of time acquired from five separate regions of the CLEAr Lens. All panels have the same units and scale. In regards to the five regions: N: nasal, T: temporal, S: superior, I: inferior, and C: central. As with the previous recordings voids have been left in place of the failed recording, but this time no asterisk has been used to mark them.

Statistical analysis of the data shown in Figure 26 reaffirmed that variation between corneal potentials was not uniformly distributed across the CLEAr Lens. Again using Welch's t-test, we showed differences between the superior and inferior distributions to be statistically significant ($p=0.053$). A similar comparison between the nasal and temporal distributions was also found to be significant ($p=0.0057$).

Next, we sought to further resolve this asymmetric behavior and brought our analysis down to the resolution of single electrodes to highlight the spatial differences in corneal potentials. We accomplished this by using a paired-difference approach, but did not average the differences as we did when calculating mean differences via Eq. 1. Upon computing the pair-wise differences we tabulated them into matrices called *topographic signatures*. We obtained one topographic signature for each run. These topographic signatures compared each electrode to all other electrodes, and since we had 30 functioning electrodes assumed the shape of 30x30 matrices. Taken as a complete 24-run set, the topographic signatures contained a total of 21,600 individual elements. Accordingly, we compressed the topographic signatures into a single 30x30 matrix via averaging across all 24 runs. This provided a template representation of the average meERG response topography. In this regard, the topographic signatures serve as numerical

means to investigate the cornea's electrical topography. This template topographic signature has been plotted as a heat map in Figure 27.

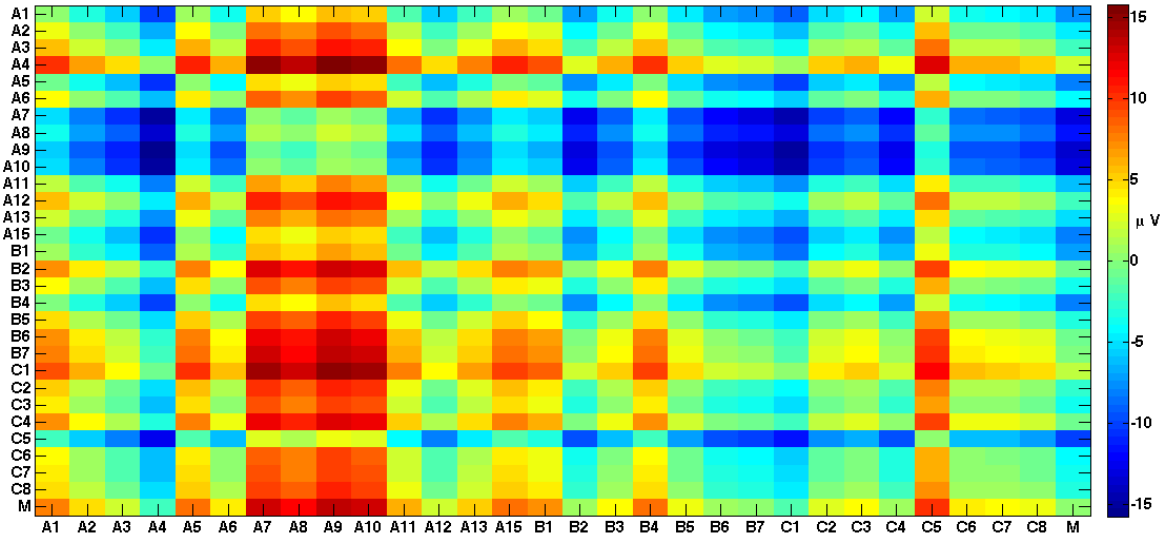

Figure 27: Heat map of average topographic signature. Both horizontal and vertical axes represent individual electrodes. The colors are mapped to average (i.e. across all runs) potential differences between the electrodes and dictated by row-column pairs. When viewing the plot, following a row across will provides differences relative to the current column's electrode. For example, A4 is *higher than* A1. Following the rows on the other hand provides an opposite interpretation, and the previous example would be changed to saying A1 is *lower than* A4.

5.3.5. Temporal Comparison of Multi-Electrode Electroretinogram Response Topographies

How consistent were the meERG response topographies over our set of 24 sequentially recorded runs? If the lens settling process and/or PoLTF thinning occurs primarily within the initial period following lens insertion we expected that topographic signatures obtained from later responses would be more similar to the average representation (Figure 27), than those obtained from early runs. In previous sections of this Results chapter we have shown that the spread of a-wave amplitudes was substantially reduced in the latter half of the recording session. Thus we sought to examine if this effect carried over to our topographic comparisons. We computed mean topographic signatures for the first and second halves of the recording session and again plotted them as heat maps (Figure 28A and B). Subsequently, we computed the difference between these two average topographic signatures and plotted the results via a heat map (Figure 28C).

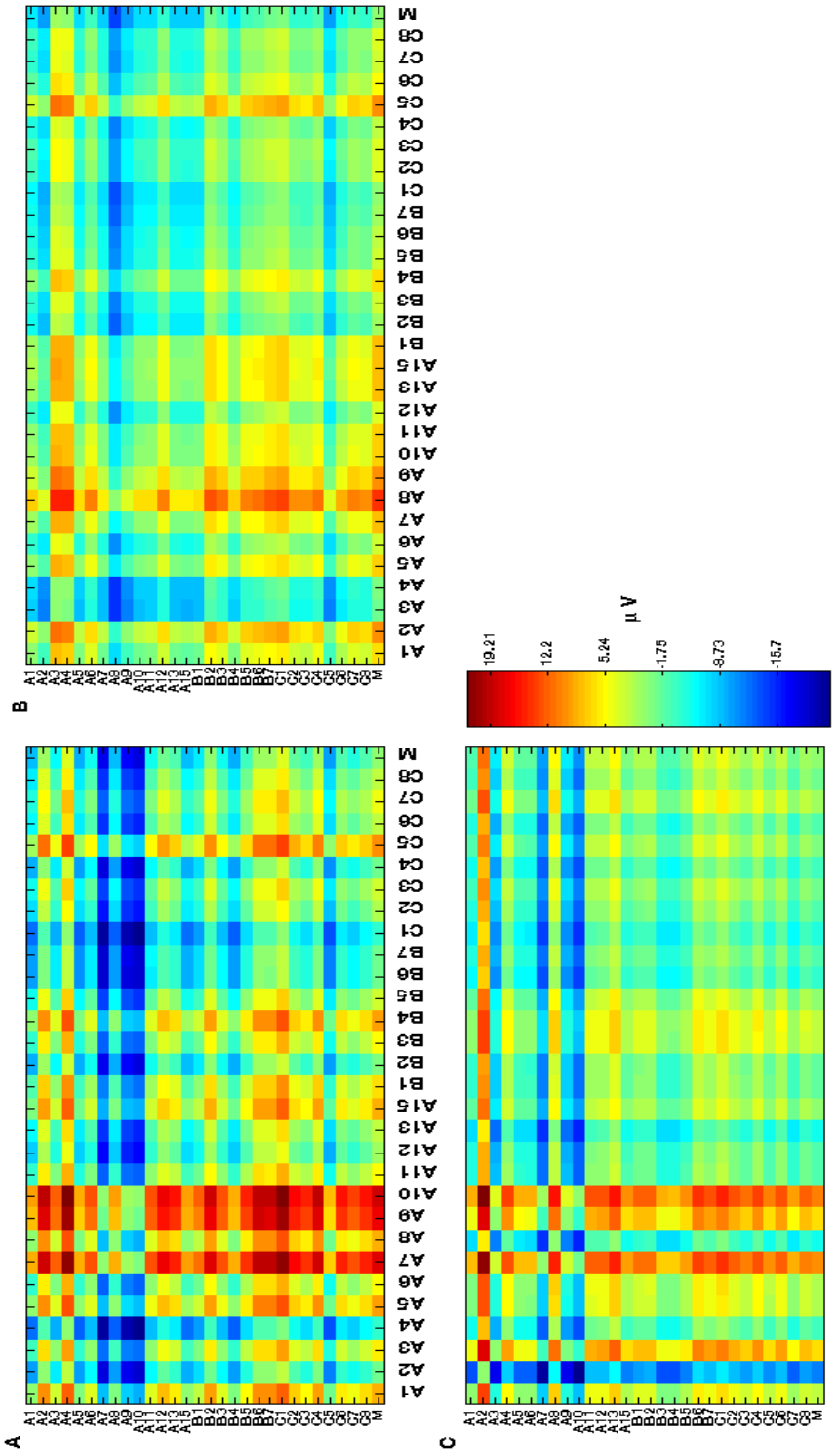

Figure 28. Average topographic signatures from the first and second halves of recording session are different. (A) shows a mean topographic signature of the *first* 12 meERG responses. (B) shows a mean topographic signature of the *last* 12 responses of our recording session. (C) shows a *difference signature* between the average shown in (A) and the average shown in (B), and has been plotted to highlight changes between the early and late halves of the recording session. Reading panel (C) **column-wise**, cool colors indicate the electrode has decreased its average amplitude from the first to the second half of the recording session (e.g. A2), while hot colors indicate that the electrode has increased its average amplitude during the second half (e.g. A10).

This provided illustrative evidence that the former and latter halves of the recording session did indeed possess different topographic signatures (Figure 28C). However, these results provided no information at the level of individual runs and are thus temporally limited. To expand upon this approach we computed pair-wise differences between our entire set of topographic signatures. These differences between topographic signatures were taken to be an indicator of similarity; low difference values signified similar electrical topographies whereas higher values showed the opposite. This approach yielded 24^2 *difference signatures* (i.e. matrices) each containing many individual values. To reduce the numerical volume of this analysis, average values for each *difference signature* was computed and referred to as *differences scores*. Having associated every pair-wise combination of runs with a single-valued *difference score,* we were able to effectively visualize how the similarity between runs changes as over time by creating a heat map of *difference scores* (Figure 29).

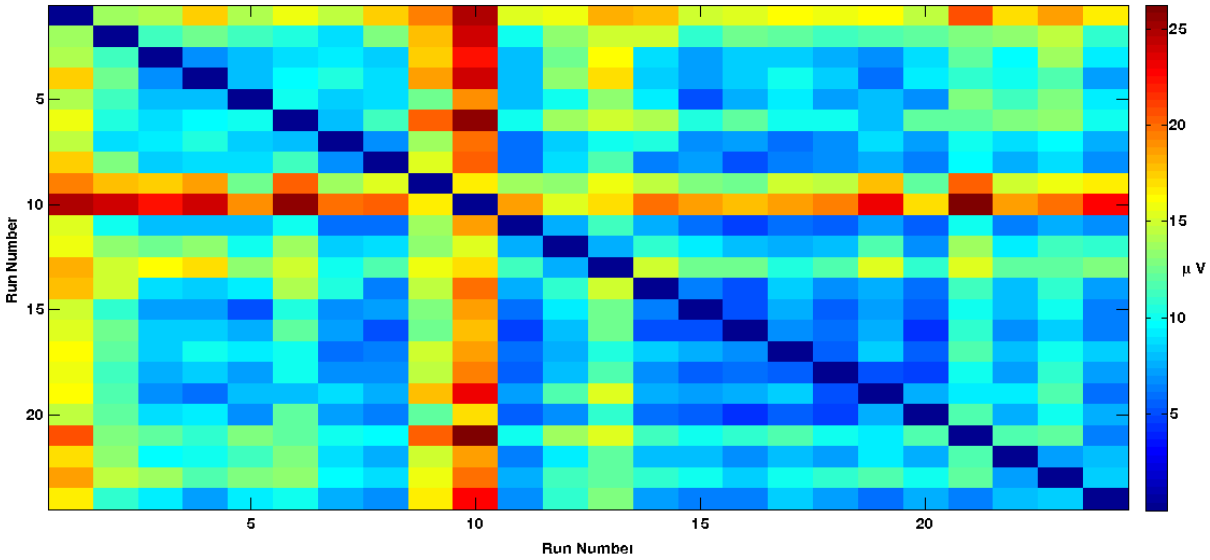

Figure 29. Difference score heat map. The above described difference score matrix is shown as a heat map above. The heat map serves as an indicator of run-to-run repeatability. Following the main diagonal, similar runs are highlighted by rectangles of bluish hues; this effect is most notable from runs 3-8 and runs 14-24. Furthermore, runs that were very dissimilar from the majority of other runs are denoted by stripes of reddish colors.

5.3.6. Orientation of Multi-Electrode Electroretinogram Response Topographies

Do the orientations of meERG response topographies change as a function of time? Using our initial hypothesis that a thickened tear film would cause the signals to become electrically shunted together we

searched our topographic signatures for exceptionally low values (i.e. <0.2 uV), indicating that that a pair of electrodes was measured to be at *almost* the same potential. Electrode pairs meeting the above criterion were tallied and the locations of the electrodes were recorded.

By recording the locations of the *nearly* equipotential electrode pairs, we could add spatial insight to our analysis by drawing connecting lines between them. Furthermore, we sorted the pairs temporally by separating the 24 runs into four groups of six runs. In doing so we were able to visually assess how the spatial orientation might change as a function of time. This was accomplished by creating a planar representation of how the electrodes are distributed about the spherically shaped cornea, and drawing the aforementioned connecting lines between them; the results are displayed in Figure 30. From Figure 30 can be observed that the number equipotential pairs increases in the second half of the recording session. Accordingly, we sought to see how the number of equipotential pairs changed as a function of time, and counted the number of pairs present in each run (Figure 31). Notably, the later runs show more equipotential pairs than do the early runs. This result fits nicely with the previously observed decrease in spatial amplitude distribution. However simply drawing and counting these lines provided limited spatial insight.

To remedy this deficit we quantified our approach by computing the angles along with the *equipotential* lines were orientated. The angles were computed between 0 and 90 degrees because we were only concerned with orientation with respect to either the nasal-temporal and superior-inferior axes. Per the orientation provided in Figure 30, angles near 0 degrees signified a nasal-temporal orientation while those near 90 indicated a superior-inferior alignment.

Upon computing the average headings (i.e. angles) of the equipotential connecting lines, we used their measures to roughly depict how meERG responses were spatially orientated. Initially we hypothesized that the cornea's electrical topography would be radially uniform, and show no preference to either a superior-inferior or nasal-temporal orientation. To test this hypothesis, we compared the angles computed from our data with a set drawn from a uniform distribution ranging from 0 to 90 degrees. This comparison

was done for both the former and latter halves of the recording session, as well as the entire 24-run session. The results were plotted as histograms (Figure 32). Angles near 0 degrees were indicative of a nasal-temporal topographical orientation, whereas angles closer to 90 degrees were representative of superior- inferior orientation. The results in Figure 32 indicate that the majority of our equipotential connecting lines orientate themselves along a heading that favors the nasal-temporal axis. This suggests that the cornea's electrical topography has tends toward a superior-inferior gradient. Comparing the two angle distributions (measured and simulated) via a paired t-test we obtained a p-value of 0.02, indicating that are measured values are indeed statically different from randomly orientated case. Also, rather interestingly, the orientation appears to be consistent between the first and second halves of the recording session (Table V).

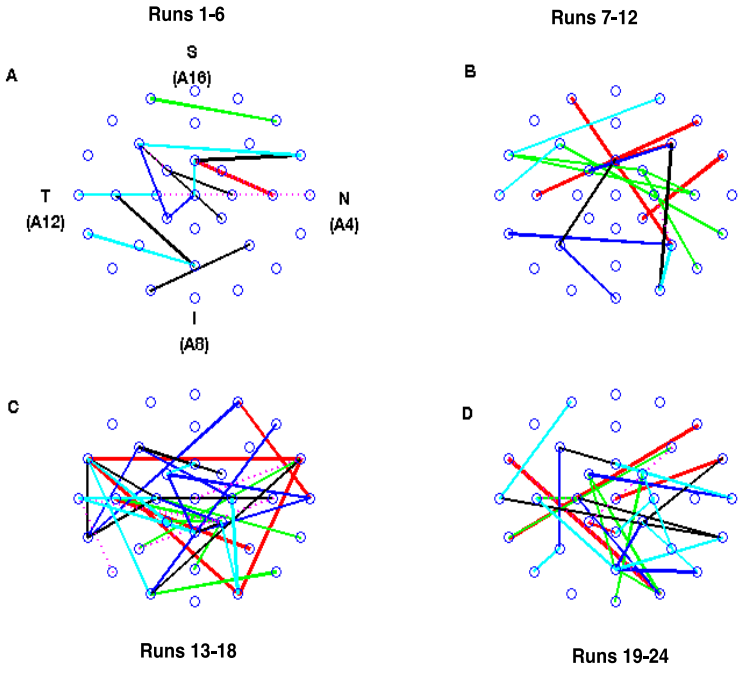

Figure 30. Line connecting nearly equipotential electrodes. The orientation of the lens for all panels is the same as labeled in (A). N,T,S,I, stand for nasal, temporal , and inferior respectively. The electrodes in parentheses give reference to which electrode each circle represents. The different color lines represent individual runs. (A) shows, for runs 1-6, lines connecting electrodes having nearly the same a-wave amplitude during given run. (B), (C) and (D) illustrate the same information as (A), but for runs 7-12, 13-18, and 19-24 respectively.

5.3.7. On-line Method For Monitoring Multi-Electrode Responses for Tear Film Induced Artifacts

Artifacts from a thickened tear film and/or the lens settling process are assumed to adversely affect the ability of multi-electrode electroretinography to assess retinal function. Thus we have proposed an on-line

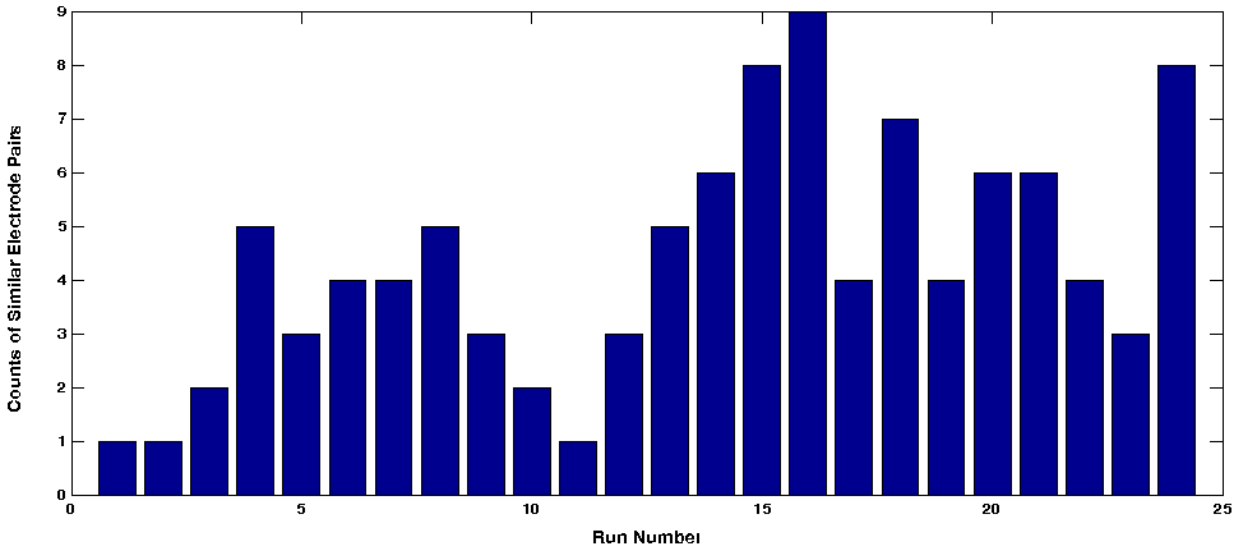

Figure 31. Counts of nearly equipotential electrode pairs. Similar electrode pairs have been counted for every run and displayed graphically above to highlight increasing similarities present in the latter runs.

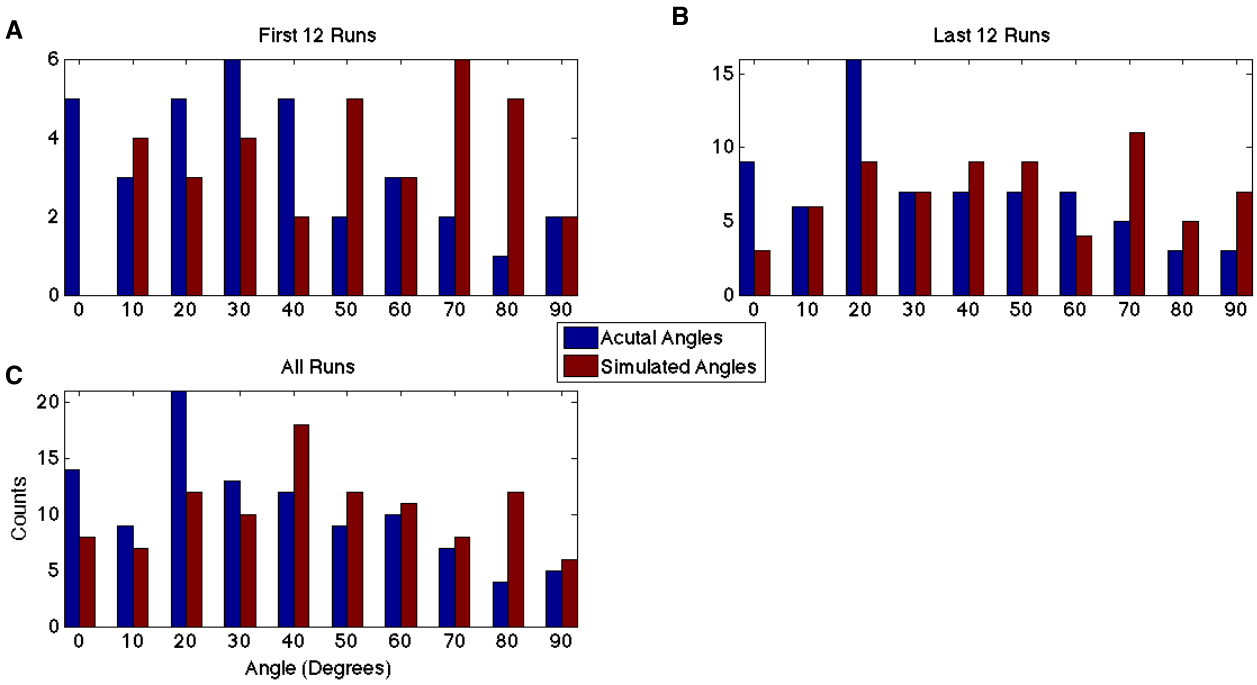

Figure 32. Equipotential lines connecting electrode pairs orientate themselves preferentially toward the nasal-temporal axis. The above plots compare our measure angles to those drawn from a random

TABLE V
AVEARGE ANGLE MEASURES OF CONNECTING LINES

All Runs (Mean±S.E.M)	**First 12 Runs** (Mean±S.E.M)	**Second 12 Runs** (Mean±S.E.M)
35.64±25.06	35.18±25.40	35.86±25.07

method through which meERG responses can be screened for these artifacts during the course of a recording session. In toward this goal, we sought a very simplistic approach that can hopefully be modified after more experiments have been conducted. The basis of our method relies upon a comparison between the most recently recorded run and the entire set of all previously collected runs (Eq. 3). Our approach assumes no *a priori* knowledge about the average electrical topography and relies heavily upon a cumulative running average calculated for the sequentially recorded runs. Additionally, we exponentially weighted differences between the current run and the three most recent runs. This was done to place extra emphasis on short-term repeatability and to ensure we could calculate an accurate QI within the first few runs, without having to wait for the cumulative average to 'settle'. This was especially important because we did not have a normative data set available for comparison. This approach places importance upon the ability of multi-electrode electroretinography to collect similar results from response-to-response; an anticipated characteristic of sequentially recorded meERG responses. Accordingly we calculated the QI for runs 3-24 according to Eq. 3 and displayed the results in Figure 33.

Notably, the early runs suffer from a low QI, but subsequently increase with time. To verify this increase, the data shown in Figure 33 was fitted with a monotonically increasing logarithmic trend line possessing an R^2 value of 0.56. However, this does not explain the low QI values associated with the early runs. This effect could possibly be due to the running average being skewed for early runs. To investigate this possibility we evaluated recording quality by an alternative *post hoc* method in which each run was compared to all the others. In this *post hoc* approach we compared runs only to the mean response found by averaging across all 24 runs. Also, to match the units of our QI, the inverse of these *average differences* has been taken, with the base unit in both cases being uV^{-1}. However, the summation of terms dictated by Eq. 3 implies inflates the QI score above that of the average difference. According, the

average difference has been similarly inflated by adding 3 additional terms. The results for the two competing approaches are shown side by side in Figure 34.

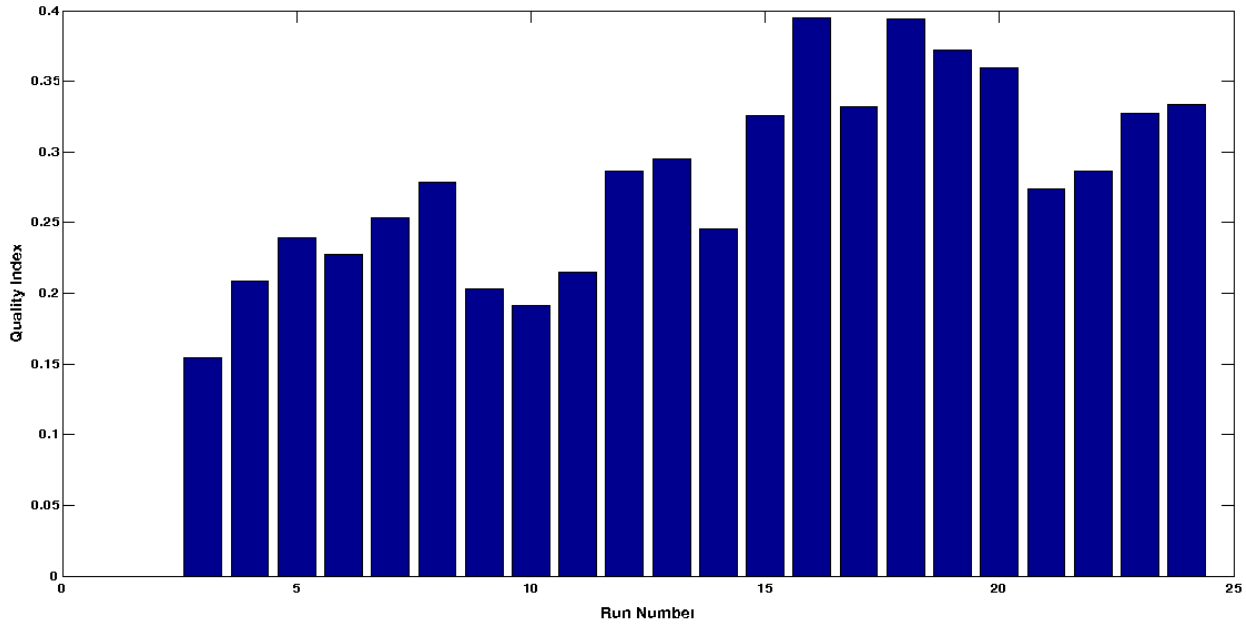

Figure 33. Quality index for runs 3 through 24 shows an increasing trend with run number. This trend is verified by fitting the above data with an increasing logarithmic trend line, see text.

Interestingly, the results provided in Figure 34 suggest that the QIs obtained via our on-line method lag those of the *post hoc* approach, especially for the early runs. To numerically examine this observation, we fit a trend line to the first 5 QIs obtained using each approach (runs 3-7 on-line method[7] and runs 1-5 *post hoc* alternate approach). The results are displayed in Figure 35 and show that the two approaches yield very similar, yet shifted, results. Thus, our proposed on-line approach can be said to lag the alternative *post hoc* method. Moreover, if we take the results of the *post hoc* method to be an accurate predictor of recording quality, the initial runs do in fact appear to suffer from a reduction in quality. However at the current time, limited insight is available to explain the mechanisms that might explain such a phenomenon. In this regard, further recording sessions will be needed to investigate these findings more thoroughly.

[7] Recall that in Eq. 3, we relied upon having runs to compare with. Hence the reason we could not assess the QI of the first two runs using this approach.

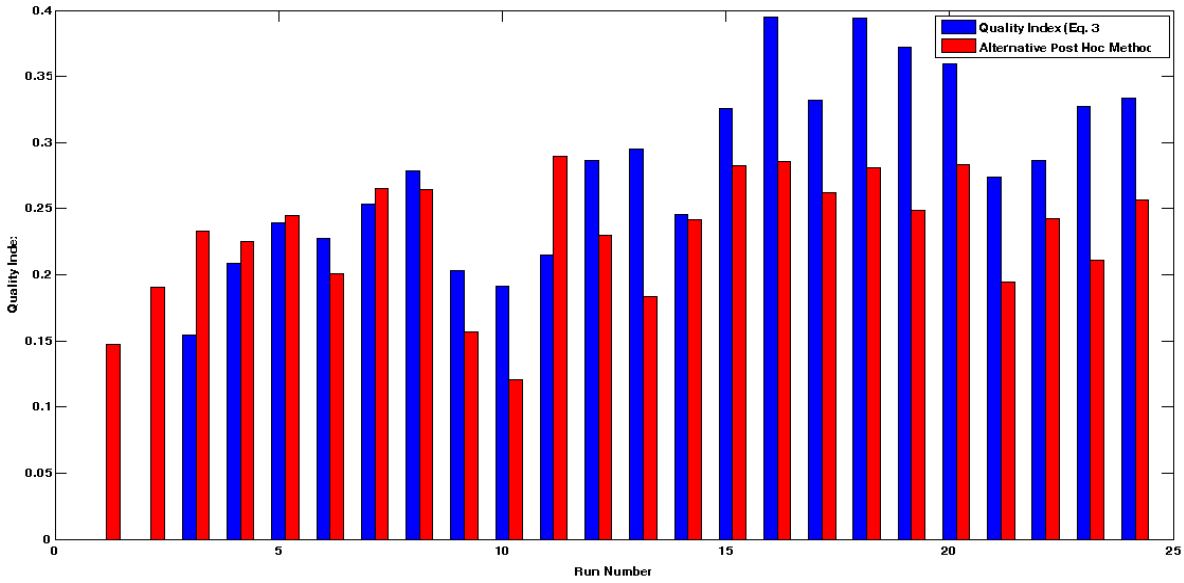

Figure 34. Comparison of quality index methods indicate similar results across approaches. The blue bars show the quality index as calculated in Figure 32. The red bars demonstrate a post hoc method of calculating the QI, in which the average from all available runs was used throughout as opposed to the running average approach.

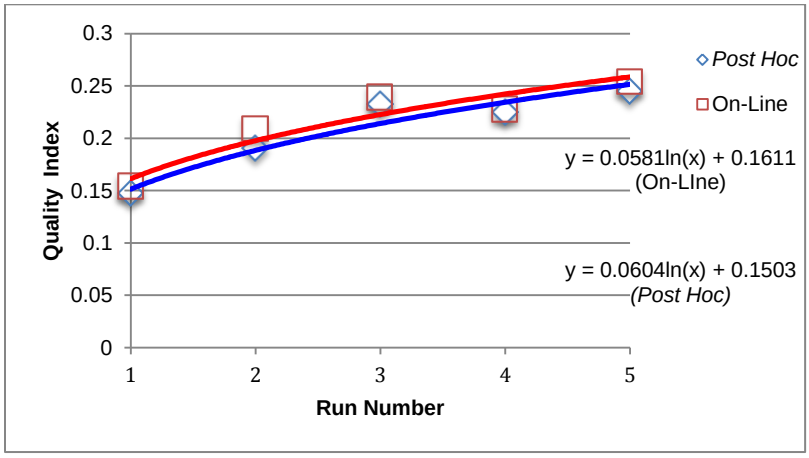

Figure 35. Proposed on-line method and alternate *post hoc* approach yield similar yet shifted results. The plot above displays the QI values for the first 5 runs measured via each approach. Recall that the on-line method did not begin until run 3 whereas the *post hoc* approach began with run 1. The on-line QI values have been shifted left by two runs; this has been done to highlight the similarity in the trend lines despite the shift. For further verification of the similarity compare the two equations are the right.

5.4 Results Summary

In section 5.1 we reviewed our CLEAr Lens analogs. Notable differences between the CLEAr Lens and both types of analogs were presented. Section 5.2 was devoted toward displaying the results of our OCT imaging experiments conducted using both types of analog lenses. Surprisingly, we found no evidence of

tear film thinning over a 20-minute period of wear with either lens. Though, we did we a marked difference in PoLTF thickness when comparing the thickness beneath the superior and inferior quadrants of the lens (Tables II and III). In Section 5.3 we presented results pertaining to our meERG analysis through which we initially probed meERG responses for spatiotemporal changes that might be related to the lens settling process. We found that significant changes in the variability of a-wave amplitudes between the first and second halves of the recording session (Figures 22 and 23, and Table IV). Subsequently we endowed our variance analysis with a spatial component and found response variability to spatially asymmetric (Figure 26). Continuing our spatiotemporal analysis we showed that the meERG response topography changes in time, and noted that changes occurred primarily on the peripheral electrodes (Figure 28). Interestingly, we found that despite these topographic changes, the orientation of the meERG responses did not vary considerably as a function of time (Figure 32). Lastly, we sought to evaluate the quality of sequentially recorded meERG responses based upon the premise that responses evoked with identical stimuli should exhibit a trial-to-trial similarity. This evaluation showed that response quality increased as a function of time (Figure 33), and was validated by comparison with a *post hoc* method (Figures 34 and 35). The implication of the aforementioned results will now be discussed.

6. DISCUSSION

6.1 Discussion of Primary Results:

6.1.1. Implications of Differences Between the CLEAr Lens and the Analogs

In accordance with Specific Aim 1, we designed and made two types of CLEAr Lens analog. Differences between the actual CLEAr Lens and the analogs used in the OCT imaging experiments may have caused a significant departure from the CLEAr Lens scenario. Neither analog had through-holes; they were left out as a consideration for imaging. Moreover, we assumed based upon previous studies into tear film dynamics (e.g. Braun, 2012) that tear fluid would flow from beneath the lens in a manner that is tangential to the corneal surface. However, neither of the analogs demonstrated a PoLTF that underwent substantial thinning (Figures 14 and 15). Thus, it appears that in the absence of blinking, the passive forces outline in Section 3.4 are not sufficient to extrude tear film from beneath our analog lenses. This was especially concerning in the case of the PMMA analog that was made very similarly to the actual CLEAr Lens. Possibly this indicates that the PoLTF beneath the CLEAr Lens is in fact several hundred micrometers thick. Imaging experiments using an actual CLEAr lens will be needed to determine this. Should this be the case, serious considerations will have to be put toward redesigning the CLEAr Lens to allow the PoLTF to thin in the absence of blinking.

The subject who wore all three lenses reported that wearing the CLEAr Lens was different from the other two; the CLEAr Lens seemed to ‘cup’ the cornea more tightly and became difficult to remove after ~20 of wear; also, the CLEAr lens caused vision to become blurred and out of focus for several minutes following lens removal (personal communication, John Hetling). This was not reported in the case of either analog. Furthermore, in previous meERG recording sessions, the CLEAr Lens has been shown to leave a circular indentation about the corneal surface (personal communication, John Hetling). No such indentations were found upon removing the analog lenses. These differences make it plausible that the CLEAr Lens creates a scenario that is unique from the analog lenses, and raises the notion that the

PoLTF beneath the CLEAr Lens to be considerably thinner than the range of 300-400 μm measured beneath our analogs.

Another point of difference between the analogs and the actual CLEAr Lens is the method of insertion. In the case of meERG recording, the subject's head is held upright by a chinrest as the lens is placed upon the subject's eye. When performing the imaging experiments with the PDMS and PMMA lenses, we chinrest was not used. This allowed the subject to tilt their head into toward the lens, a movement we observed the subject to make as the lens was inserted. By changing the angle of the head upon lens insertion, it is possible that different amounts of tear solution remained in the lens each time it was inserted. Consequentially, there is a possibility that the above mentioned differences in lens insertion might have caused the PoLTF beneath our analogs be thicker than what is usual in the case of meERG recording using the CLEAr Lens.

Our overall goal in using CLEAr Lens analogs was to mimic the CLEAr lens case while using lenses better suited for the task of imaging. But in regards to the previously discussed reasons, it is reasonable to assume we did not effectively mimic the CLEAr Lens scenario. To improve upon these efforts it is suggested that an actual CLEAr Lens be used for future OCT imaging experiments, and that the lens be inserted with the aid of a chin rest.

6.1.2. **Notable Conclusions from Imaging Experiments**

Per Specific Aim II another goal was to measure the tear film thickness beneath our CLEAr Lens analogs in the ~20 minutes that followed lens insertion. We hypothesized that the PoLTF would be initially thick and subsequently thin due to the lens settling process. However in the case of both the PDMS and PMMA analogs, the PoLTF did not become thinner. Especially surprising was the thickness of the PoLTF we that we observed; the thinnest central PoLTF was measured to be 322 μm. This is significantly greater than the PoLTF measured in previous studies. For example, in Chen *et al.* (2010) the maximal PoLTF thickness following lens insertion was found to be 15.4 μm.

Interestingly, we observed different PoLTF thicknesses beneath PMMA and PDMS analogs. A possible cause for this difference in thickness could be incongruences of material properties between the two lenses. The PDMS lens was less stiff and less hydrophobic (Table I) than the PMMA lens. Aside from these material differences, an alternate argument for this finding is that upon lens insertion, the two lenses contained different amounts of tear solution. The drops used to fill the lenses were not metered. Thus, the volume of solution placed into the lens cup prior to insertion was likely different for each lens, and as discussed above, this might have impacted our PoLTF thickness measurements.

Contrasting with our hypothesis that the PoLTF would thin over time, we instead observed the PoLTF to become thicker in the first few minutes following lens insertion (Figure 14 and 15). This effect is not likely due to an influx of tear fluid beneath the lens. Such an effect might explainable by the position of lens shifting as a function of time. Alternatively, this observed increase in PoLTF thickness could have been caused by changes in OCT scan location. When acquiring the OCT images, the device was positioned to scan across a line that bisected the pupil. And as seen in Figure 17, the pupil appears to become dramatically smaller during the course of the image session. This reduction in pupil size may have caused the position of the scan to change relative to the lens. Thus the observed thickening in PoLTF might represent an artifact that is attributable to our images being obtained from different positions of the lens. In support of this claim, the horizontal lines in Figure 17 which denote the position of the OCT line scans appear to be located on different positions of the lens.

Nonetheless, both images in Figure 17 show the lens to have a position that is slightly off-center. This off-center positioning of the lens may have produced the observed superior-inferior asymmetry in PoLTF thickness. It would have been beneficial to see if this asymmetry changes as a function of time by measuring a time-series of sequentially acquired images as we did for the central thickness. However we did not acquire enough sequential images orientated about the superior-inferior axis, especially in the first few minutes of the imaging following lens insertion[8]. Moreover, even if sequential images were acquired

[8] In both imaging sessions, the images were first acquired about the nasal-temporal axis. This is unfortunate, because the thickening in tear film we observed happed in the several minutes following lens insertion, a time over which we acquired no images about the superior-inferior axis.

superior-inferior axis, slight changes in scan position could affect the measurements. Thus it is recommended that future experiments scan locations be referenced to the lens itself as opposed to the pupil, and that the orientation of the scans (i.e. superior-inferior or nasal-temporal) remain fixed for the duration of each imaging session.

In regards to why the lens would assume an off-center position with respect to the cornea, we speculate that uneven pressure from the eyelids may be to blame. Further evidence for uneven eyelid pressure upon the lens is provided in Figure 18, which shows that the greatest amount of corneal reshaping occurred beneath the upper and lower edges of the both the PDMS and PMMA analog lenses. Interestingly, the fact the reshaping was slightly more pronounced on the inferior cornea than the superior cornea. This effect was surprising and could be explained by the lower eyelid exerting a complimentary upward force upon the lens to hold the lens in place upon the eye. Furthermore, eyelid morphology has been previously shown to influence corneal shape (Read *et al.,* 2007). Combining this evidence it appears plausible that eyelids are pressing with considerable force against the both the upper and lower edges of the lens. And while we can only speculate as to what effect these forces have on tear film thickness, corneal topography measurements provide evidence they do indeed alter the shape of the cornea. Toward this end, it might be beneficial to redesign the CLEAr lens in such a way that pressure from the eyelids is minimized; this could possibly be accomplished via using a smaller diameter lens.

6.1.3. Interpretation of Multi-Electrode Electroretinogram Responses and How They Change as a Function of Time

Through collecting a time-series of meERG responses over a 25-minute window immediately following lens insertion, we sought to investigate how the lens settling process manifests itself in meERG recordings. We began by performing noise analysis to identify noise-corrupted responses (Figures 19 and 20). From these figures it was observed that the responses collected over the second half of the recording session were notable less noisy than those collected during the first half; this is especially apparent by looking at the distribution of fuchsia ‘tiles’ in Figure 20. The source of this noise, however,

remained to be determined. Possibly the noise was due to physiological factors unrelated to the electrical activity of the retina. Interestingly, the electrodes with the consistently highest noise level were primarily located inferior quadrant of the a-ring (Figure 20). This is suggests that noise level at individual electrodes could be related to their positioning on the lens and might therefore be affected by the thickness of tear film beneath the CLEAr Lens. Thus we opted to include the especially noisy responses in our subsequent analysis, and sought to examine possible links between noise, other meERG response attributes, and the lens settling process.

A noteworthy observation stemming from our noise analysis was that the runs 10,12 and 13 were found to have to multiple electrodes located in the inferior half of the peripheral A-ring that failed to meet our predetermined SNR threshold (Figure 20). It just so happens, that runs 10, 12, and 13 are associated with small, but noticeable, spikes in average a-wave amplitude. While these two observations could very well be coincidental occurrences, they raise the possibility that signal noise and signal amplitude are correlated to one another. Tear fluid consists of an aqueous component that is ionic and electrically conductive and thus might create a path for electrical activity generated in the nerves surrounding the eye to 'flow' beneath the edge of the CLEAr Lens and summate with the electrical activity generated by the retina. Accordingly, a potential scenario could arise in which an attempted blink or other eyelid movements produce enough current to increase the average a-wave amplitude for the runs in question. Furthermore, the fact that the inferior PoLTF was found to be thicker than the PoLTF beneath the central and superior regions of the lens supports the notion that the hypothetical effect described above would be localized to the inferior A-ring electrodes. This is indeed the case for the noise levels we recorded, and in this regard, it may be plausible that thickened PoLTF might serve as a potential conduit for noise to infiltrate meERG recordings.

Turning our attention away from noise and to meERG signals, we probed for possible impacts of a thickened PoLTF by evaluating the spatial amplitude distribution present in each of the meERG responses (Figures 22 and 23). This was done to investigate our hypothesis that an initially thick tear film would cause meERG signals to become electrically shunted together, thus endowing the early-on

recordings with a low degree of spatial amplitude distribution. Following the lens settling period and PoLTF thinning, we postulated that the amplitude spread of a- and b-wave amplitudes would subsequently increase.

Through inspecting the Figures 22 and 23, a temporal trend similar to that found in the noise analysis became apparent. Namely, the spatial spread of meERG a-wave amplitudes was significantly reduced during the second half of the recording session when compared to the values obtained during the first half. This temporal trend provided a strong indication that changes in meERG responses are indeed occurring over the 20-minute time window following lens insertion. Furthermore, the similarities between noise levels and amplitude spread as a function of time (i.e. run number), suggest that an unsettled lens mad adversely affect the ability of multi-electrode electroretinography to record retinal activity in a predictable manner.

Next we investigated the temporal trends of a-wave amplitudes. First plotted the average a-wave amplitude as a function of time (Figure 24), and subsequently did the same for amplitude time series at each electrode (Figure 25). Interestingly, the average a-wave amplitude increased as a function of time. While temporally telling, Figures 24 and 25 provided limited spatial insight. Thus we decided to group electrodes according to the region of the cornea they contacted. This afforded us the ability to correlate the observed spatial asymmetries in PoLTF thickness with meERG responses. We grouped the electrodes into 5 separate regions and analyzed the dispersion of a-wave amplitudes within each region (Figure 26). We noticed considerable asymmetries between the regions, and along both the nasal-temporal and superior-inferior axes. As an interesting point of note, our OCT imaging experiments also provided evidence of a similar superior-inferior asymmetry. This hints at the possibility that spatial differences in PoLTF thickness may be associated with spatial differences in amplitude distribution.

The relationships between the individual electrodes and how they changed over time, was the next area of meERG analysis we ventured into. We used the relationships between electrodes a ‘bar code’ of the cornea’s electrical topography and sought to study how this topography changed as a function of time.

We observed that that the A-ring electrodes exhibited the greatest difference between the first and second halves of the recording session. Comparatively, the B- and C-rings showed significantly less difference. Furthermore, the electrodes positioned on the inferior half of the A-ring (i.e. A7-10) displayed a decrease in a-wave amplitude when comparing the first and second halves of the recording session. Contrastingly, the superior A-ring electrodes (i.e. A14-16, A1, and A2; see Figure 9) failed to exhibit similar decreases. Electrode A2, actually showed a marked increase in relative a-wave amplitude from first to the second half, while electrode A16 showed a more modest increase. Unfortunately, two of the three unavailable electrodes happened to be located on the superior quadrant of the A-ring. Thus substantive conclusions in this regarding the behavior of the superior A-ring electrodes cannot be made from these experiments.

Next, we compared electrical topographies of individual runs. This was done assess the trial-to-trial variability of meERG responses over the 24-run recording session. The use of a stimulus that was nearly identical for all trials we postulated that the meERG responses should be very similar as well. However, we considered the possibility that the lens settling process could adversely affect the ability of multi-electrode electroretinography to function in this capacity, especially in the first several minutes following lens insertion. We found that the trial-to-trial variability to be noticeable more pronounced over the first half of the recording session compared to the second (Figure 29). Thus, despite the fact our imaging experiments provided no substantive evidence of PoLTF thinning, multiple meERG analysis approaches have indicated that considerable changes in meERG responses occur over the ~20 minutes following lens insertion. Potentially these changes in trial-to-trial variability, spatial amplitude distribution, and noise level are to some extent associated with a lens settling process.

Upon probing our meERG response data for spatial trends, we showed via Figure 27 (and A2; see Appendix), a superior-inferior asymmetry of a-wave amplitudes. The potentials measured on the inferior A-ring were consistently smaller than the electrodes at other corneal location. With our limited data, and the fact that the technique of multi-electrode electroretinography is still being developed, we sought to compare these results to an already established electroretinographic approach. Multifocal

electroretinography (mfERG) offers a comparative method by which the function of the retina can be mapped. In this alternative approach to multi-electrode electroretinography, a single electrode is used to record responses evoked from a multitude of retinal locations. By correlating these responses to the retinal regions they are thought to originate from, mfERG offers a method to spatially interpret retinal function. To this end, efforts have been made to assess the topography of the mfERG response. A prior study found that mfERG responses evoked from the superior retina were higher in amplitude than those evoked from the inferior retina (Nagatomo *et al.,* 1998). This finding seems to be in agreement with our observed superior-inferior asymmetry. However, a subsequent study found no such topographical asymmetry in mfERG responses (Verdon and Haegerstrom-Portnoy, 1998).

While this apparent disagreement in mfERG interpretation would seem to weaken our case that the observed asymmetry arises as a result of retinal function, one must take into account the differences between meERG and mfERG. *Multifocal electroretinography* uses a single electrode to map a large region of the retina while stimulating select regions. In doing so, the placement of the electrode will impact how the responses particular retinal regions are weighted. Multi-electrode electroretinography on the other hand, uses full-field stimuli to drive activity across the entire retina, and recording this activity across 33 electrodes distributed across the corneal surface. Accordingly, it is hypothesized that via recording in this manner, activity from the peripheral retina can be detected with greater resolution. Thus, it may be plausible that minor asymmetries observed in mfERG response topographies could be disregarded as insignificant. Along these lines, it is interesting to note that in the work by Verdon and Haegerstrom-Portnoy (1998), a slight superior-inferior asymmetry was observed, but was dismissed due to lack of statistical significance (Verdon and Haegerstrom-Portnoy, 1998).

Continuing along the lines of topographical analysis, we investigated how the orientation of meERG responses might change as a function of time. We found that the responses orientated preferentially toward the nasal-temporal axis (Figure 32), and that the orientation did not significantly change as a function of time (Table V). This temporal stability with respect to response orientation could indicate that

while certain electrodes exhibit varied behavior over the first half of the recording compared to the second (see Figure 28C), the response topography as a whole remains intact.

These variations in amplitude at certain electrodes were especially pronounced in the periphery (i.e. A-ring). Despite the fact the response topography as a whole seemed to remain intact, the unpredictable nature of these variations in response amplitudes negatively impacts the utility of meERG recording. Namely, in the wake of such variations, information about the function of the retina becomes distorted. Thus, we decided to develop an approach that considers all possible electrodes and scans the topography of the response for abnormalities.

Toward this pursuit, we wished to develop a computationally simple algorithm that was capable of determining the *quality* of a given response on-line, during the course of a recording session. We computed and plotted the QI scores as a function of time (Figure 32), and noticed that the scores increased with consistency over the first 15 minutes following lens insertion. This result was expected based on the results from the previous analysis. However, we took into consideration that the lack of an *a priori* average response negatively affected the QI scores of early-on runs due to the fact our algorithm relies heavily upon a running average. Accordingly we decided to compare our method (i.e. Eq. 3) with an alternative *post hoc* approach that that did not use a running average, but instead relied only upon comparing the current run to the average of all the other responses. The results for this comparison are plotted in Figure 34 and 35 and indicate that both the algorithm described by Eq. 3 and the post hoc alternate approach yield similar results yet shifted results.

In sum, the meERG responses exhibited multiple attributes that changed as a function of time. However due to inconclusive imaging experiments we are at a loss to know whether or not these changes occurred as the result of tear film thinning and/or a lens settling process. It is hoped that future imaging experiments can shed light on this issue.

6.2. Study Limitations

Despite the fact this study did not produce a firm conclusion regarding the impact of tear film thickness on meERG responses, it made us aware of the shortcomings associated in our current approaches. The surprisingly thick PoLTF brings up the notion that there are considerable differences between our analog lenses and the actual CLEAr Lens. However until OCT images are taken through an actual CLEAr Lens, we will not know how such differences affect PoLTF thickness. Another limitation was that the amount of tear solution placed into the lens cup prior to imaging experiments was not measured and therefore introduces unnecessary experimental variability. This could have had an impact on our OCT imaging experiments, especially in regards to the different PoLTF thickness measured beneath the PDMS and PMMA analog lenses.

Another potential source of error during our OCT imaging experiments was the lack of pupil dilation. When performing meERG recordings, the pupil is dilated prior to CLEAr Lens insertion. This step was not performed when imaging as it was thought to be unnecessary. However, as was suggested in Figure 17, the pupil size changed after lens insertion; and since the pupil was used to guide OCT scan location, this could have affected our PoLTF measurements. Furthermore, this difference makes imaging results more difficult to compare with meERG responses. Thus it is suggested that in future imaging experiments that the subject's pupil be dilated prior to lens insertion. Additionally, it is recommended that a reference position on lens itself be used to determine the OCT scan location rather than the 'center-of-the-pupil' method used in present work.

The meERG portion of our experiments also contained notable deficits. Namely, all three non-functioning electrodes happened to be in the superior region of the CLEAr Lens, thus making it difficult to accurately assess superior-inferior asymmetry in meERG responses. Also, due to equipment error, we did not successfully obtain a response one-minute following lens insertion. Upon looking at Figure 24, this is a noteworthy deficit since the average amplitude of the a-wave appears to be changing quite dramatically during that time period. Furthermore, the lack of a normative human meERG data set weakened our analysis substantially, and prevented us from using evoking meaningful statistics on numerous occasions.

6.3. Future Directions

To overcome the aforementioned limitations and strengthen future studies, the following future directions are recommended. Based upon differences between the CLEAr Lens and the analogs, it appears essential that a CLEAr Lens be used in future OCT imaging experiments to accurately determine PoLTF thickness in the CLEAr Lens Scenario. This can be accomplished by using a lens with no cable attached and placing a parylene sheet over the through holes. In the present study it was noted that changes in pupil size and/or lens position could have impacted the PoLTF measurements obtained from our imaging experiments. To resolve these inconsistencies we suggest two changes for future imaging experiments: one is to apply pupil dilating drops prior to lens insertion as means of controlling pupil size; and two is to monitor position of the lens relative to the cornea. Another potential change in regards to the imaging experiments would be to use a chin rest to when inserting the lens as to more accurately match the meERG recording protocol. Also, as a means of reducing unnecessary experimental variability, it would be beneficial to meter the amount of tear solution placed into the lens cup prior to both imaging *and* meERG experiments. This would allow the volume of PoLTF to be more precisely controlled. Moreover, it would introduce greater consistency between imaging and meERG experiments and allow the results of the parallel experiments to be better correlated.

Another reasonable direction for future experiments to take is the investigate PoLTF and/or the lens settling process as a potential source of noise in meERG recordings. Currently, when meERG responses are analyzed, the noise corrupted runs are discarded without further consideration. However, to fully assess the impact that the lens settling process might have on recording such a correlation ought to be examined. Additionally, we noticed that the average a-wave amplitude changed as a function of time. We are currently at a loss to explain this this occurrence and seek to combine improved imaging studies and a *greater quantity* of available meERG response data to elucidate possible mechanisms.

8. APPENDIX

7.1 **Supplementary Results**

In the primary Results chapter, b-wave analysis was excluded due to considerably high variability. However, the following Figure highlights the similarity of temporal trends between average a- and b-wave amplitudes is included for completeness:

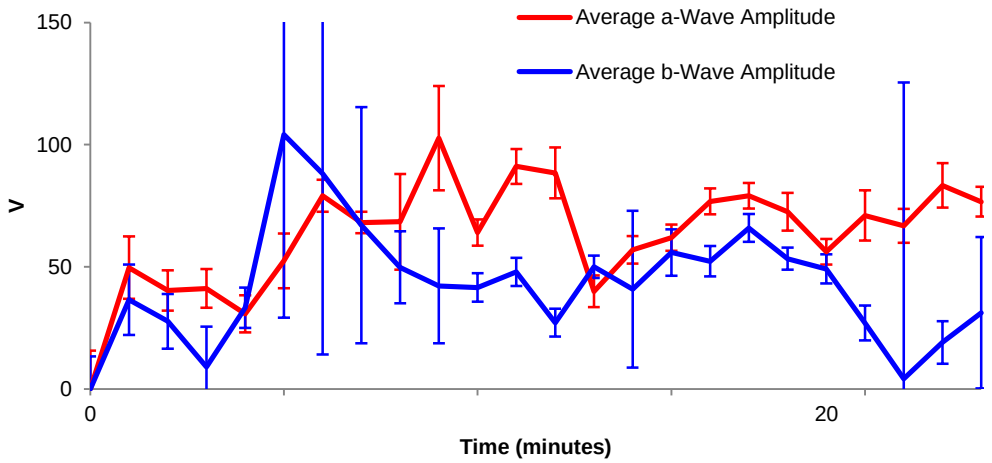

Figure A1. Comparison of variations in a- and b-wave amplitudes as a function of time. The axis at the left indicates the excursion of a- and b-wave amplitudes from their value in the initially recorded run. Actual amplitudes are not important here, only the differences between previous time points are. Hence the reason absolute a- and b-wave amplitudes were not used above.

In the main body of this Thesis we investigated the cornea's electrical topography numerically. Our rationale for doing so was to highlight trends at the level of single electrodes and not muddy the interpretation via the use of interpolated maps or other similar approaches. While numerically enlightening at the resolution of single electrodes, spatial insight can be imparted upon this approach by interpolating the topography and plotting the results as contour plots. This was done in a manner similar to the results shown in Figures 27 and 28; however for clarity the interpolated results will be shown in four separate figures. Figure A2 shows an interpolation of a-wave values averaged across *all* responses; Figure A3 shows an interpolation of a-wave values averaged across the *former* half of the recording session (i.e. runs 1-12); and Figure A4 shows an interpolated map of a-wave values averaged across the *latter* half of the recording session (i.e. runs 13-24). Subsequently we subtracted plot shown in Figure A3

from that shown in Figure A4, and plotted a *difference map* to spatially highlight the electrodes that changed most greatly between recording session halves; this is shown in Figure A5.

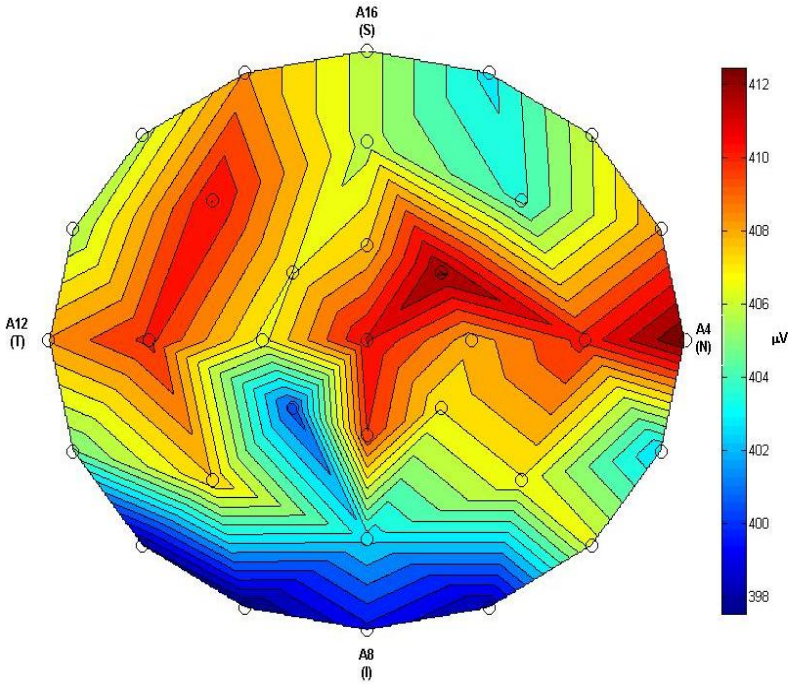

Figure A2. Contour plot of interpolated average a-wave topography. In this and the subsequent figures, black circles indicate electrode positions and orientation is same as that shown in Figure 9.

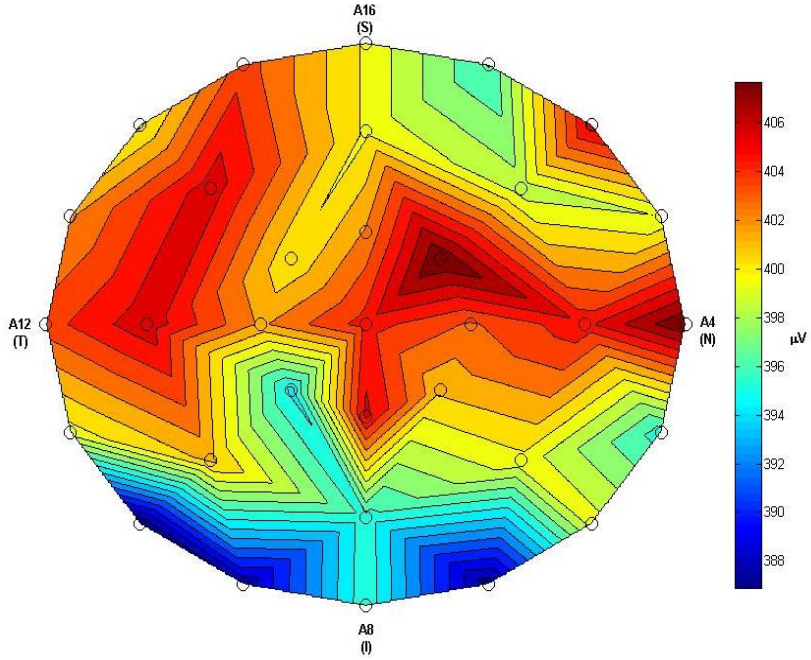

Figure A3. Contour plot of interpolated average a-wave values from first half of recording session.

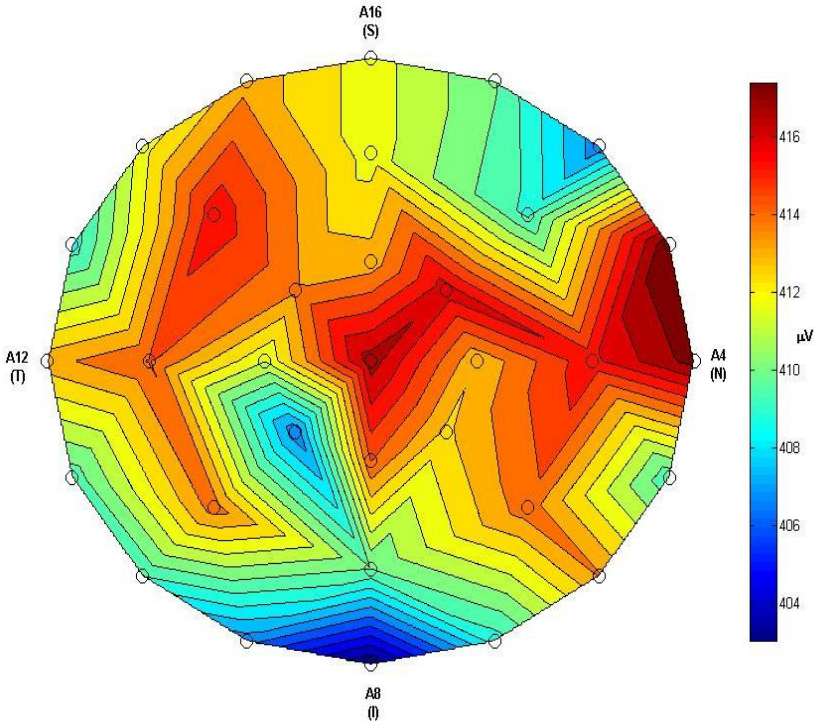

Figure A4. Contour plot of interpolated average a-wave values from second half of recording session.

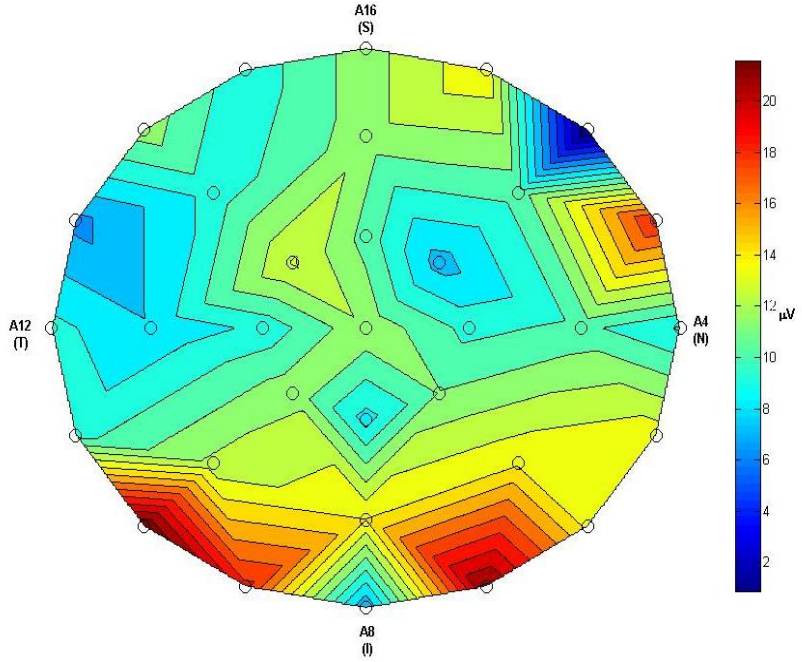

Figure A5. Difference of contour plots shown in Figures A3 and A4.

7.2 Supplementary Discussion

Figure A1 provides a firm indication that the a- and b-waves do in fact follow the similar temporal trends. Thus the approaches used in this Thesis may extend to b-wave analysis as well. However, before this occurs, the spatial variations in b-wave amplitude must be addressed. Importantly, it must be determined if these variations occur as a result of retinal or non-retinal sources. Again invoking our assumption that our identical stimulus presentations will yield repeatable results, the high variability of b-wave amplitude distributions suggests that non-retinal sources might play a prominent role. A possibility to consider is that the stimulus evoked occasional eye movements and/or blinks which affected only the later stages of the response (i.e. the period after the a-wave depression). Though, this suggestion may be refuted by claims that any stimulus evoked artifacts should occur after the retinal signal processing cascade has reached higher brain centers for further processing. In this regard, a previous study using turtle retina has shown that current injections into photoreceptors take around 100 ms to elicit a maximum ganglion cell response (Baylor and Fettiplace, 1977). This is far greater than the latency by which the b-wave follows stimulus onset.

An alternative suggestion is that the subject becomes aware of the stimulus even before light onset and can voluntarily respond differently to each stimulus presentation. The subject is made aware of the stimulus presentation by virtue of the trigger switch, which engages the recording software 100 ms prior to light onset. When switched on, the switch emits an audible ‘click’ that the subject can hear. Thus the subject knows with a good deal of precision when the stimulus flash is to occur and can pre-emptively respond if he or she chooses to do so. A proposed method to correlate any eye movements and/or blink attempts with meERG responses would be to place a skin electrode beneath the lower eyelid and record the response. Any movements, even attempted ones, should be detectable by this electrode. Moreover, the responses of this skin electrode can be temporally matched to meERG responses, thus allowing the effects of motion artifacts to be studied more intimately. Such an approach could be quite useful in redesigning meERG recording protocols in such a way that motion artifacts are minimized.

Figures A2-A5 show interpolated electrical topographies about a two-dimensional corneal surface. As predicted by the topographic signatures, electrodes A7-10 show a-wave values that are depressed

compared to the rest of the electrode population. This is especially apparent in Figure A2. Upon comparing Figure A2 with Figure 18, the depression in amplitude (i.e. the inferior blue region) lies in a similar location to the area of the inferior cornea underwent corneal reshaping (i.e. the lower red region in Figure 18). This provides further evidence that eyelid pressure might be affecting meERG responses. However, we cannot provide a firm answer as why electrodes A7, A9, and A10 displayed prominent amplitude increases between recording session halves. Such an effect could be due to the lens settling process, but future imaging experiments using the actual CLEAr Lens are needed to further investigate this possibility.

CITED LITERATURE

Azartash, K., Kwan, J., Paugh, J. R., Nguyen, A. L., Jester, J. V., & Gratton, E. (2011). Pre-corneal tear film thickness in humans measured with a novel technique. *Molecular vision*, *17*, 756

Bach, M., Unsoeld, A. S., Philippin, H., Staubach, F., Maier, P., Walter, H. S., ... & Funk, J. (2006). Pattern ERG as an early glaucoma indicator in ocular hypertension: a long-term, Prospective study. *Investigative ophthalmology & visual science*, *47*(11), 4881-4887.

Banitt, M. R., Ventura, L. M., Feuer, W. J., Savatovsky, E., Luna, G., Shif, O., ... & Porciatti, V. (2013). Progressive loss of retinal ganglion cell function precedes structural loss by several years in glaucoma suspects. *Investigative ophthalmology & visual science*, *54*(3), 2346-2352.

Baylor, D. A., & Fettiplace, R. (1977). Kinetics of synaptic transfer from receptors to ganglion cells in turtle retina. *The Journal of physiology*, *271*(2), 425-448.

Benedetto, D. A., Shah, D. O., & Kaufman, H. E. (1975). The instilled fluid dynamics and surface chemistry of polymers in the preocular tear film.*Investigative Ophthalmology & Visual Science*, *14*(12), 887-902.

Begley, C. G., Chalmers, R. L., Abetz, L., Venkataraman, K., Mertzanis, P., Caffery, B. A., ... & Simpson, T. (2003). The relationship between habitual patient-reported symptoms and clinical signs among patients with dry eye of varying severity. *Investigative ophthalmology & visual science*, *44*(11), 4753-4761.

Berger, R. E., & Corrsin, S. (1974). A surface tension gradient mechanism for driving the pre-corneal tear film after a blink. *Journal of biomechanics*, *7*(3), 225-238.

Berson, E. L. (1993). Retinitis pigmentosa. The Friedenwald Lecture.*Investigative ophthalmology & visual science*, *34*(5), 1659-1676.

Braun, R. J. (2012). Dynamics of the tear film. *Annual Review of Fluid Mechanics*, *44*, 267-297.

Bron, A. J., Tiffany, J. M., Gouveia, S. M., Yokoi, N., & Voon, L. W. (2004). Functional aspects of the tear film lipid layer. *Experimental eye research*, *78*(3), 347-360.

Bui, B. V., & Fortune, B. (2004). Ganglion cell contributions to the rat full-field electroretinogram. *The Journal of physiology*, *555*(1), 153-173.

Chen, Q., Wang, J., Tao, A., Shen, M., Jiao, S., & Lu, F. (2010). Ultrahigh-resolution measurement by optical coherence tomography of dynamic tear film changes on contact lenses. *Investigative ophthalmology & visual science*,*51*(4), 1988-1993.

Craig, J. P., Willcox, M. D., Argüeso, P., Maissa, C., Stahl, U., Tomlinson, A., ... & Stapleton, F. (2013). The TFOS International Workshop on Contact Lens Discomfort: Report of the Contact Lens Interactions With the Tear Film Subcommittee. *Investigative ophthalmology & visual science*, *54*(11), TFOS123-TFOS156.

Doane, M. G. (1988). In vivo measurement of contact lens wetting. *Journal of the British Contact Lens Association*, *11*, 110-111.

Ehlers, N. (1965). The thickness of the precorneal tear film. *Acta Ophthalmol (Copenh)*, *81*, 92-100.

Gipson, I. K. (2004). Distribution of mucins at the ocular surface. *Experimental eye research*, *78*(3), 379-388.

Harris MG, Mandell RB. (1969) Contact lens adaption:Osmotic theory. *American Journal of Optometry and Archives of the American Academy of Optometry, 46*, 196–202.

Holt, V. (1997). *Laser induced fluorescence measurement of the tear film thickness under a contact lens* (Master's Thesis). Retrieved from: http://hdl.handle.net/1721.1/43429

King-Smith, P. E., Fink, B. A., Fogt, N., Nichols, K. K., Hill, R. M., & Wilson, G. S. (2000). The thickness of the human precorneal tear film: evidence from reflection spectra. *Investigative ophthalmology & visual science*, *41*(11), 3348-3359.

King-Smith, E., Fink, B., Hill, R., Koelling, K., & Tiffany, J. (2004). The thickness of the tear film. *Current eye research*, *29*(4-5), 357-368.

Korb, D. R., Weber, W. L., Chinnock, R. B., Gravely, B. T., Grenon, S. M., & Zelina, M. (2012). *U.S. Patent No. 8,215,774*. Washington, DC: U.S. Patent and Trademark Office.

Lehmann, D., & Skrandies, W. (1980). Reference-free identification of components of checkerboard-evoked multichannel potential fields.*Electroencephalography and clinical neurophysiology*, *48*(6), 609-621.

Little, S. A., & Bruce, A. S. (1995). Osmotic determinants of postlens tear film morphology and hydrogel lens movement. *Ophthalmic and Physiological Optics*, *15*(2), 117-124.

Mao, Y., Flueraru, C., Chang, S., Popescu, D. P., & Sowa, M. G. (2010). Imaging of biomedical turbid tissue using catheter swept-source optical coherence tomography. In *Medical Measurements and Applications Proceedings (MeMeA), 2010 IEEE International Workshop on* (pp. 151-157).

Nagatomo, A., Nao-i, N., Maruiwa, F., Arai, M., & Sawada, A. (1998). Multifocal electroretinograms in normal subjects. *Japanese journal of ophthalmology*,*42*(2), 129-135.

Nichols, J. J., King-Smith, P. E., Hinel, E. A., Thangavelu, M., & Nichols, K. K. (2012). The use of fluorescent quenching in studying the contribution of evaporation to tear thinning. *Investigative Ophthalmology & Visual Science*,*53*(9), 5426-5432.

Nickells, R. W., Howell, G. R., Soto, I., & John, S. W. (2012). Under pressure: cellular and molecular responses during glaucoma, a common neurodegeneration with axonopathy. *Annual review of neuroscience*, *35*, 153-179.

Owen, M. J., & Smith, P. J. (1994). Plasma treatment of polydimethylsiloxane.*Journal of adhesion science and technology*, *8*(10), 1063-1075.

Phelan, J. K., & Bok, D. (2000). A brief review of retinitis pigmentosa and the identified retinitis pigmentosa genes. *Mol Vis*, *6*, 116-124.

Quigley, H. A., & Broman, A. T. (2006). The number of people with glaucoma worldwide in 2010 and 2020. *British Journal of Ophthalmology*, *90*(3), 262-267.

Read, S. A., Collins, M. J., & Carney, L. G. (2007). The influence of eyelid morphology on normal corneal shape. *Investigative ophthalmology & visual science*, *48*(1), 112-119.

Sharma, A. (1998). Breakup and dewetting of the corneal mucus layer. In*Lacrimal Gland, Tear Film, and Dry Eye Syndromes 2* (pp. 273-280). Springer US.

Smith, J. A. (2007). The Epidemiology Subcommittee of the International Dry Eye Workshop (2007), The epidemiology of dry eye disease: report of the epidemiology subcommittee of the international dry eye workshop (2007). *Ocul. Surf*, *5*, 93-107.

Tan, B., Zhou, Y., Svitova, T., & Lin, M. C. (2013). Objective Quantification of Fluorescence Intensity on the Corneal Surface Using a Modified Slit-lamp Technique. *Eye & contact lens*, *39*(3), 239-246.

Tyagi, G., Collins, M. J., Read, S. A., & Davis, B. A. (2012). Corneal changes following short-term rigid contact lens wear. *Contact Lens and Anterior Eye*,*35*(3), 129-136.

van Velthoven, M. E., van der Linden, M. H., de Smet, M. D., Faber, D. J., & Verbraak, F. D. (2006). Influence of cataract on optical coherence tomography image quality and retinal thickness. *British journal of ophthalmology*, *90*(10), 1259-1262.

Verdon, W. A., & Haegerstrom-Portnoy, G. (1998). Topography of the multifocal electroretinogram. *Documenta Ophthalmologica*, *95*(1), 73-90.

Viswanathan, S., Frishman, L. J., Robson, J. G., Harwerth, R. S., & Smith, E. L. (1999). The photopic negative response of the macaque electroretinogram: reduction by experimental glaucoma. *Investigative ophthalmology & visual science*, *40*(6), 1124-1136.

Wang, J., Fonn, D., Simpson, T. L., & Jones, L. (2003). Precorneal and pre-and postlens tear film thickness measured indirectly with optical coherence tomography. *Investigative ophthalmology & visual science*, *44*(6), 2524-2528.

Wang, J., Jiao, S., Ruggeri, M., Shousha, M. A., & Chen, Q. (2009). In situ visualization of tears on contact lens using ultra high resolution optical coherence tomography. *Eye & contact lens*, *35*(2), 44.

VITA

MATTHEW ELLIS

EDUCATION

University of Illinois at Chicago

M.S in Bioengineering (in progress) **2014 (intended date)**

Thesis Project: Investigation of Ocular Surface via Two Methods: 1) At present I am working in a lab primarily focused on developing a novel method for recording electroretinograpic potentials from multiple sites on the cornea via a multi-electrode contact lens. In this regard, my focus is to evaluate the tear film dynamics underneath this lens. This project is motivated by the notion that the tear film must be sufficiently thin for distinct potentials to be across the ocular surface. 2) Using the aforementioned multi-electrode lens, I was involved in a project that sought to measure corneal impedance at multiple locations. The main goal of this investigation is to correlate mechanical changes associated with corneal damage with changes in electrical impedance. The ultimate hope is to develop a non-invasive way to monitor one's corneal health, a technology that will be of particular importance when monitoring the cornea after the LASIK procedure and for the diagnosis of corneal diseases such as keratoconus. Advisor: John R. Hetling, PhD.

Additional work: Over the last year, I designed and built a computer-controlled chromatic stimulus source for use in electroretiography experiments. With the device now operational, it may be useful in further validating the novel technology of multi-electrode electroretinography via the inclusion of chromatic stimuli.

Future Educational Plans:

Following the conclusion of my Bioengineering M.S. program the University of Illinois at Chicago I will begin working toward a PhD in Neuroscience at the University of Southern California, where I intend to focus my studies upon the retina. This transition between institutions is scheduled to occur in the summer of 2014.

Northern Illinois University

B.S. in Applied Physics **2010**

Area of Concentration: I took considerable coursework in electricity and magnetism and electronics. Concurrently I developed a strong interest in bioelectricity and led to a marked interest in neuroscience and biophysics.

Minor: Biochemistry

Undergraduate Research Project: Over the course of two years I worked in a transmission electron microscopy laboratory with Dr. Yasuo Ito of Argonne National Laboratory and Northern Illinois University. The primary focus of the project was to examine the material properties of newly developed substances such as high temperature superconductors. However in the second year the project was given an interesting twist in which we took stereo image stacks to allow for a three dimensional depiction of our sample. This subsequent project took third place at the Northern Illinois University Undergraduate Research Day.

AWARDS

Outstanding Physics Senior Award (2010): An award given to the Physics student whom the faculty deemed displayed excellence in Physics during their tenure at Northern Illinois University.

Dean's Award (2010): Awarded to the undergraduate Physics student graduating with the highest grade point average.

RELATED EXPERIENCE

Northwestern University, Laboratory of Dr. Steven DeVries
Lab Technician, Summer Internship **June 2011 – August 2011**
While working with Dr. DeVries I was introduced to the laboratory techniques of immunohistochemistry and briefly to patch clamp electrophysiology. The context of the research was to classify the types of OFF bipolar cells contained within the ground squirrel retina. Specifically, my focus was associated with the immunohistochemistry aspect of the research, where, after fixation, I mounted and imaged both whole-mount retina and retina slices via confocal microscopy.

MEMBERSHIPS

Association for Research in Vision and Ophthalmology, Student member, January 2013 - Present